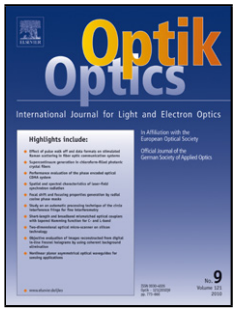

Title: Influence of surface modification on enhancement of luminescent properties of SiO_2@$SrTiO_3$:Dy^{3+} nanopowders: Probe for visualization of sweat pores present in latent fingerprints

Authors: A. Sandhyarani, R.B. Basavaraj, G.P. Darshan, H. Nagabhushana, M.K. Kokila

PII: S0030-4026(18)32012-6
DOI: https://doi.org/10.1016/j.ijleo.2018.12.088
Reference: IJLEO 62105

To appear in:

Received date: 28 November 2018
Accepted date: 18 December 2018

Please cite this article as: Sandhyarani A, Basavaraj RB, Darshan GP, Nagabhushana H, Kokila MK, Influence of surface modification on enhancement of luminescent properties of SiO_2@$SrTiO_3$:Dy^{3+} nanopowders: Probe for visualization of sweat pores present in latent fingerprints, *Optik* (2018), https://doi.org/10.1016/j.ijleo.2018.12.088

Influence of surface modification on enhancement of luminescent properties of SiO_2@$SrTiO_3$:Dy^{3+} nanopowders: Probe for visualization of sweat pores present in latent fingerprints

A. Sandhyarani[1, 2], R.B. Basavaraj[3], G.P. Darshan[4], H. Nagabhushana[3, *], M.K. Kokila[2]

[1]*Department of Physics, Govt. Science College, Bengaluru 560 001, India*
[2]*Department of Physics, Bangalore University, Bengaluru 560 056, India*
[3]*Prof. C.N.R. Rao Centre for Advanced Materials, Tumkur University, Tumkur 572 103, India*
[4]*Department of Physics, Acharya Institute of Graduate Studies, Bengaluru 560 107, India*

[*]Corresponding author: +91- 9945954010, E-mail address: bhushanvlc@gmail.com (H. Nagabhushana).

Abstract

The paper reports, novel SiO_2@$SrTiO_3$: Dy^{3+} (5 mol %) nanopowders fabricated via the low temperature sonochemical route by utilizing bio-surfactant *Aloe Vera* gel extract. The powder X-ray diffraction results display intense and narrow peaks confirm the monoclinic phase of $SrTiO_3$. The photoluminescence emission spectra of $SrTiO_3$:Dy^{3+} (5 mol %) with different layers of SiO_2 coating display intense and characteristic peaks at ~ 483 nm ($^4F_{9/2} \rightarrow {}^6H_{15/2}$), 576 nm ($^4F_{9/2} \rightarrow {}^6H_{13/2}$) and 664 nm ($^4F_{9/2} \rightarrow {}^6H_{11/2}$). The broad thermoluminescence glow peak with maximum intensity at ~ 200 ^oC for both with and without coated $SrTiO_3$:Dy^{3+} (5 mol %) nanopowders was noticed. The optimized SiO_2@$SrTiO_3$:Dy^{3+} (5 mol %) nanopowders was most suitable for visualization of the latent fingerprints, revealing explicit specific ridge characteristics, including level I -III. Therefore, the present work opens a new possibility of use of prepared nanopowders for WLEDs, visualization of latent fingerprints and dosimetry applications.

Keywords: Sonochemical route; Silica coating; Photoluminescence; Thermoluminescence; Latent fingerprints.

1. Introduction

The surface modified nanopowders (NPs) with fine-tuned morphology create numerous interest for the researchers due to its many scientific and industrial applications [1]. Generally, the surface defects may hindrance the various properties of the NPs. To overcome from such a problem, the core-shell materials with nano/micron size were extensively used owing to its tunable sizes and inexpensive than other materials [2-5]. As a consequence, silica was extensively used as a surface modifier due to its outstanding chemical stability, optical transparency, certainly thickness controllable shell, low cytotoxicity and biocompatibility [6]. Hence, silica modified NPs acts as a luminescent probe and offers many possible applications in the fields, namely immunoassaying, DNA sequencing and clinical diagnosing. In addition, silica modified NPs can avoid renal filtration, results for long habitation time in the bloodstream, which gives sufficient information of diseased tissues [7].

Till date, many host materials were reported in the literature. Among, strontium titanate ($SrTiO_3$) was considered to be novel host for low-voltage electron-excitation displays and white LEDs applications because of its wide energy band gap (3.3-4.5 eV) nature and chemical and compositional stability at harsh environment [9]. In addition, $SrTiO_3$ based materials offers many potential applications, namely dynamic random access memory, tunable microwave gadgets, photo-electrodes for hydrogen production, hydrogen storage etc. [8-11]. Among various RE ions, the Dy^{3+} ions were used as activator ions in many inorganic hosts generating white light by appropriately regulating blue as well as yellow emissions. Additionally, dopant Dy^{3+} ions were highly sensitive probe because their luminescence originates from the 5D→4F transitions and crystal field can influence easily on the 5D State [12-14].

Various synthesis techniques were employed for the preparation of $SrTiO_3$ hosts, including solid state reaction, solution combustion synthesis, ultrasonication, hydrothermal, solvothermal, sol-gel etc. [15-17]. However, the ultrasonication method was considered as

facile, operated under ambient conditions, low cost method, able to obtain high homogeneity and easily scalable to industry requirements [18]. Because of high temperature and partial pressure acoustic cavitation destroys the attractive forces of molecules and leads to nanopowders [19]. Sonochemistry emerges from acoustic cavitation; the formation, development, and implosive crumple of the bubbles. The collapse of these bubbles was relatively adiabatic in nature results in huge energy liberation from the bubble leading to bottom up approach. This route was simple, single step approach and can be worked in ambient conditions. Further advantages of this technique were high purity, narrow size distribution, nanoparticles with uniform shapes able to obtain and fast reaction rate. Additionally, it brings down the crystallization temperature, rapid synthesis and low effective cost enables for easily scalable to industrial needs [20].

Precise radiation dose delivery was of critical importance in the treatment of cancer. Thermoluminescence (TL) was one of the important study in order to precise measurement of ionizing radiations. TL studies play a key role in order to obtain the kinetic parameters, namely trap depth (b), activation energy (E) and frequency factor (s). Further, these parameters provide vital information about the TL mechanism as well as trap level distribution in the NPs. The NPs exhibiting excellent response to the ionizing radiations (UV, γ, β, etc.) were used in the TL dosimeters (TLDs) dosimeters in various fields, namely medical, environmental monitoring, personal dosimetry, neutron dosimetry, etc. Further, high sensitivity at low ionizing radiation doses, wide range of linear response with dose, good stability and reproducibility were some of the prerequisite conditions for the fabrication of TLDs. Therefore, for materials scientists it has become a great challenge to fabricate high quality TLD NPs which exhibit all the above properties [21-27].

Generally latent fingerprints (LFPs) are the most advantageous types of physical proof for demonstrating personality. The improvement in visualization of LFPs was normally based on

the utilization of a chemical substance or a powder material that makes a difference between the finger mark residue and the substrate [28-30]. Nanoparticle-based materials have pulled an attention to this application in view of their substantial surface region and high illumination. In any case, the vast majority of these samples do not have a long-term stability, which reflected in a poor protection of the LFPs and high background hindrance. A couple of reports have demonstrated that the surface alteration of silica covered materials with functional organic groups can enhance the LFP identification [31, 32].

Hence, in the present work novel $SrTiO_3:Dy^{3+}$ (5 mol %) (STD) NPs were prepared by ultrasonication route using Aloe Vera gel extract as a bio-surfactant. The prepared sample was modified with SiO_2 by following Stober method. The effect of various coating levels on photoluminescence (PL) and TL properties were extensively studied. The prepared $SiO_2@SrTiO_3:Dy^{3+}$ (5 mol %) NPs (SO@STD) were used to visualize LFPs on various surfaces, including porous/non-porous surfaces. The level-III ridge details (i.e., sweat pores) were clearly revealed in (SO@STD) NPs stained LFPs.

2. Experimental

2.1. Synthesis of STD NPs

The STD NPs was prepared by using stoichiometric quantities of Strontium chloride [$SrCl_2$, (Sigma Aldrich 99.9 %)], Titanium (IV) chloride [$TiCl_4$, (Sigma Aldrich 97 %)] and Dysprosium (III) chloride hexahydrate [$DyCl_3.6H_2O$, (Sigma Aldrich, 99.9 %)] and Aloe Vera gel extract (as a bio-surfactant) was thoroughly dissolved in double distilled (DD) water (~100 ml) using a magnetic stirrer. The resultant reaction solution was treated with ultrasound using titanium made horn probe sonicator by adjusting ultrasonic frequency ~ 20 kHz and power ~ 300 W. After a certain time, the reaction mixture undergoes precipitation and obtained product was washed and filtered many times using DD water and alcohol. The resultant powder was dried at the ~ 80 ^oC for 1 h and further calcined at ~ 800 °C for 3 h.

2.2. Coating STD NPs with SiO_2

The standard Stöber method was followed for coating [33]. The stoichiometric amounts of fabricated STD NPs were thoroughly mixed in 50 ml of absolute ethanol by using an ultrasonic probe sonicator for ~ 1 h. The 30 ml of ammonium hydroxide solution and 1 ml of TEOS were added slowly in a dropwise to the above resultant solution. The final reaction mixture was thoroughly mixed using a probe sonicator for ~ 3 h in an ice bath. The precipitate obtained at the end of the reaction was centrifuged, washed several times and dried in a hot oven at the ~ 80 °C for 8 h. The obtained product was calcined at ~ 600 °C for 4 h. Further, in order to produce thin layers of SiO_2, the same coating protocol was used in varying TEOS concentration (2 ml and 3 ml). Schematic diagram to demonstrate synthesis of SO@STD NPs was depicted in Fig.1.

2.3. Characterization

Shimadzu (model no -7000) diffractometer was used to analyze the product confirmation and structural analysis. Scanning electron microscope (Hitachi, Model No. TM-3000) and transmission electron microscope (Hitachi, Model No. H-8100) were used to examine the morphological features of the prepared NPs. Diffuse reflectance (DR) measurements were recorded using a Perkin Elmer (Lambda-65) Spectrometer. Raman spectra were recorded by using Mono Vista CRS Raman spectrometer (S & I). PL measurements were carried out using Horiba Fluorolog-3, modular Spectrofluorimeter. TL studies were carried out using the Nucleonix TLD reader (model TL 1009I) after irradiating the samples with ^{60}Co γ - rays in the dose range 1- 8 KGy.

2.4. Visualization of LFPs

The forensic related substrate surfaces, including porous/non-porous/semi-porous were selected and cleaned thoroughly using ethanol and dried in a normal environmental conditions. The hands of the FP volunteers were washed with soap and water. The washed hands were

rubbed on the nose and forehead region. Then, the hands were impressed on the various surfaces. The obtained FP was not visible to the naked eye and hence it called as LFPs. The optimized SO@STD NPs was stained on the LFPs by a smooth brushing activity. The processed LFPs were photographed by using DSLR Canon EOS 100D camera with 5 mm focal points (SIGMA MACRO, 50 mm, F2.8, EXDG) under normal light. Further, we conducted various experiments, namely LFPs aging, environment temperature, etc. to evaluate the efficiency of NPs and powder dusting technique.

3. Results and discussion

3.1. PXRD analysis

Fig.2 depicts the PXRD profiles of STD NPs and SO@STD with the coat I-III NPs. The profiles display intense and narrow peaks, which confirm the monoclinic phase of $SrTiO_3$ and were good agreement with a standard JCPDS No. 79-0176. No significant changes observed in the PXRD profiles with an increase of SiO_2 coating (Fig.2). The average crystallite size and strain present in the prepared samples were estimated by using both the Scherrer's and Williamson –Hall's (W-H) relation [34];

$$D = \frac{0.9\,\lambda}{\beta \cos\theta} \qquad \text{---------- (1)}$$

$$\beta \cos\theta = \varepsilon\left(4 \sin\theta\right) + \frac{\lambda}{D} \text{ ---------- (2)}$$

where 'β'; full width at half maximum of the peaks (FWHM in radian), 'λ'; X-ray wavelength (1.542 Å), 'ε'; the strain in the sample, 'D'; crystallite size and 'θ'; Bragg's angle. The estimated values of ε and D for the prepared samples were tabulated in Table 1.

3.2. Diffuse reflectance (DR) studies

DR spectra of the STD and SO@STD NPs were depicted in Fig.3 (a). The spectra display many electronic absorption bands at ~ 320, 348, 364, 381, 796, 887 and 1071 nm, due to $^6H_{15/2} \rightarrow {}^4I_{11/2}$, $^6H_{15/2} \rightarrow {}^6P_{7/2}$, $^6H_{15/2} \rightarrow {}^4I_{13/2}$, $^6H_{15/2} \rightarrow {}^6F_{5/2}$, $^6H_{5/2} \rightarrow {}^6F_{7/2}$ and $^6H_{5/2} \rightarrow {}^6F_{9/2} + {}^6H_{7/2}$

transitions of Dy^{3+} ions, respectively [35]. The optical energy gap (E_g) of the prepared samples was estimated by using Kubelka–Munk theory by using following equations [36];

$$F(R_\infty) = \frac{(1-R_\infty)^2}{2R_\infty} \text{ ---------- (3)}$$

$$h\nu = \frac{1240}{\lambda} \text{ ---------- (4)}$$

where R_∞; reflection co-efficient of the sample, λ; absorption wavelength. The energy band gap plots of STD and SO@STD NPs was depicted in Fig.3 (b). The calculated value of the E_g were given in Table 1. A slight increase in the E_g value with SiO_2 coatings was clearly noticed.

3.3. Raman spectral studies

Fig. 4 shows the Raman spectra of STD and SO@STD NPs recorded at room temperature. The spectra exhibit characteristic modes at ~ 149, 177, 289, 482, 545, 730, 795 and 1073 cm^{-1}, which were attributed to TO_1, TO_2, TO_3, LO_2, TO_4, TO LO_4 and $SrCO_3$, respectively [37]. A noticeable increase in the intensity of TO_2 and LO_2 modes in thick layered SiO_2 coated samples was noticed. This enhancement was due to creation of Sr site vacancies induced by SiO_2 coatings.

3.4. Morphological studies

SEM micrographs of STD and SO@STD NPs was shown in Fig.5. It was evident that the dumbbell shaped particles were observed for STD samples (Fig.5 (a)). However, agglomerated and fused particles were observed in the thick SiO_2 coated samples (Fig.5 (b-d)). From TEM images the shell SiO_2 and STD NPs can be easily distinguished Fig.6 (a-d). The enlarged portions of TEM indicate the thickness of SiO_2 coating on the phosphor. It was found that the thickness of the SiO_2 layer of the phosphor was increased with increase in SiO_2 coatings and it was found to be ~ 0.3, 0.5 and 0.8 nm for a coat I-III, respectively. In addition, the interplanar spacing (d) between lattice planes were measured in HRTEM and found to be ~ 0.32 nm for

(211) plane (Fig.6 (e)). The well crystallinity of the sample was further confirmed by SAED patterns (Fig.6 (f)).

3.5. PL studies

Generally, the interaction of SiO_2 shell and core may cause substantial changes in the PL properties. Many literatures were available on the effect of coatings on the PL emission intensity, but the results were quite controversial [38-47]. The effect of SiO_2 coating on the PL properties of the previously reported results was listed in Table 2. In the present work, the PL behavior of the prepared samples was systematically studied. Fig.7 (a) shows the PL excitation spectrum of STD NPs by monitoring emission wavelength of ~ 576 nm in the range 325 – 500 nm. The sharp and intense peaks observed at ~ 324, 351, 363, 385 and 422 nm, which were attributed to $^6H_{15/2} \rightarrow {}^6P_{7/2}$, $^4I_{13/2}$, $^4G_{11/2}$, $^4I_{15/2}$ and $^4F_{9/2}$ transitions of Dy^{3+} ions, respectively. Fig.7 (b) shows the PLE spectra of SO@STD NPs excited at 351 nm. The spectra exhibit intense and characteristic peaks at ~ 483 nm ($^4F_{9/2} \rightarrow {}^6H_{15/2}$), 576 nm ($^4F_{9/2} \rightarrow {}^6H_{13/2}$) and 664 nm ($^4F_{9/2} \rightarrow {}^6H_{11/2}$) [48]. The inset of Fig.7 (b) shows the variation plot of PL intensity versus SiO_2 coating layers. It was clearly observed that the PL intensity was found to increase with coating numbers. The enhancement in the PLE intensity was mainly due to passivation of surface states and reduced surface defects of the NPs after coatings. Controversially, the diminished PL emission intensity with coating was reported literature. The decrement in the PL intensity was due to many reasons, namely reduced excitation light power reaching the core as a consequence of scattering and reflection of light by the shell, the reduction in core content per unit volume of the sample and silanol groups present in the sample which act as luminescence quenchers. Fig.7 (c) shows the energy level diagram of Dy^{3+} ions in the $SrTiO_3$ host.

The photometric properties of the STD and SO@STD NPs were estimated. It was noticed that the estimated International Commission on Illumination (CIE) coordinate values were situated in the white region of the chromaticity diagram [49]. Further, correlated color

temperature (CCT) values were also estimated using the standard relation described elsewhere [50]. The CIE, CCT diagrams and their corresponding coordinates were given in (Fig. 7 (d & e)). In addition, the color purity of prepared samples was estimated using following relation [39];

$$color\ \ purity\ (CP) = \frac{\sqrt{(x_s - x_i)^2 + (y_s - y_i)^2}}{\sqrt{(x_d - x_i)^2 + (y_d - y_i)^2}} \times 100\% \quad \text{--------- (5)}$$

where (x_s , y_s) and (x_d , y_d); coordinates of a sample point and dominant wavelength and (x_i , y_i) ; co - ordinates of the illuminated point. The photometric properties (CIE coordinates, CCT values and CP) of the synthesized samples were estimated and listed in Table 3. The aforementioned results clearly evident that the prepared samples may quite useful for white component in WLEDs applications.

Fig.8 shows decay profiles of STD and SO@STD NPs. The decay data of STD NP was well-fitted with mono-exponential equation as given below [51];

$$I = A_1 \exp(-t/\tau_1) \quad \text{---------- (6)}$$

where I_1; PL intensity at t intervals of time and τ_1; lifetime of an excited energy state. The $\tau_{average}$ was calculated by using the following equation:

$$\tau_{average} = \frac{I_1 \tau_1^{\,2}}{I_1 \tau_1} \quad \text{---------- (7)}$$

In addition, the decay data of SO@STD NPs can be well fitted using a tri-exponential function as follows:

$$I = A_1 \exp(-t/\tau_1) + A_2 \exp(-t/\tau_2) + A_3 \exp(-t/\tau_3) \quad \text{-------- (8)}$$

where I_1, I_2, and I_3; PL intensities at three different time intervals and τ_1, τ_2 and τ_3; lifetimes in an excited energy state. The $\tau_{average}$ of SO@STD NPs was calculated by using a following equation;

$$\tau_{average} = \frac{I_1\tau_1^{\,2} + I_2\tau_2^{\,2} + I_3\tau^2{}_3}{I_1\tau_1 + I_2\tau_2 + I_3\tau_3} \quad \text{---------- (9)}$$

The average lifetime of STD and SO@STD with I-III coat NPs was estimated and found to be 14.45, 17.12, 19.32 and 23.42 ms, respectively. The increase in the decay time was mainly due to decreased non-radiative relaxation caused by elimination of day–OH groups and reduction of refractive index of the sample of SiO_2 coating.

3.6. TL studies

3.6.1. Effect of γ-dose on the TL glow curves

Fig.9 (a) shows the TL glow curves of STD and SO@STD NPs under 1 kGy γ-dose. A single glow peak at ~ 200°C was observed. From the figure it was evident that no noticeable change in the glow peak shape, however two-fold enhancement in the intensity was observed. Further, the highest TL intensity was observed in the coat III sample. Fig.9 (b) shows the variation plot of TL intensity versus SiO_2 coatings.

The optimized SO@STD with III coated NPs was irradiated with various γ-ray dose (1-8 kGy) and its TL response was shown in Fig.9 (c). The spectra exhibit a uniquely broad, intense peak centered at ~ 200 °C. Fig.9 (d) evident that superior linearity was observed in lower γ-ray doses (up to 4 kGy), while a further increase of γ-ray doses (4-7 kGy) product exhibit sub-linear nature. Saturation behavior was noticed with further increase of γ-ray dose.

3.6.2. Effect of heating rate on the SO@STD NPs

The effect of various heating rates (3 - 6 $^oC/s$) on TL glow curves of SO@STD with coat III NPs were systematically studied and shown in Fig.10 (a). With an increase in the heating rate, the intensity of the TL glow curve decreases. As the heating rate was increased from 3 - 6 $^oC/s$, glow peak temperature was shifted towards higher temperature side (from 200 ^oC to 230 ^oC). These changes can be explained based on the fact that at lower heating rates the charge carriers responsible for producing the required luminescence and have sufficient time to get re-trapped

at the recombination center. However, with increase of heating rate, non-radiative type thermal quenching happened as a result of charge carriers recreated from the traps which cannot recombine at recombination center and energy was transferred via a non-radiative transition. Therefore, TL intensity may suppress for higher heating rates.

3.6.3. Computerized glow curve deconvolution (CGCD)

The TL glow curve was associated with the various trap levels lying in between the conduction and valence band of a solid. To know the levels of different trap by estimating different kinetic parameters, namely E, b and s. The comprehensive dosimetric evidence of TL material was considered based on the above parameters. Therefore, CGCD and Chen's glow peak shape method were used to estimate the kinetic parameters which were highly essential to get the trap levels [52].

The TL glow curve of SO@STD with coat III coat and 8 kGy irradiated NPs was deconvoluted using CGCD method (Fig.10 (b)). The kinetic parameters of each trap level were estimated for each respective deconvoluted using TL_{anal} computer program [53]. The theoretically generated glow curves were fitted with those obtained from experimental glow curves. The quality of fitting was tested by estimating the figure of merit (FOM) for each fitting defined by following relation:

$$FOM = \frac{\sum TL_{Exp} - TL_{The}}{\sum TL_{The}} \quad \text{---------} \quad (10)$$

Here, TL_{Exp}; TL intensity of experimental and TL_{The}; TL intensity of theoretical glow curves respectively. The summation extends over all the available experimental data points. The quality of fitting and choice of appropriate number of peaks was refined by repeating the process of fitting in order to get the minimum FOM with minimum number of possible peaks. FOM values were acceptable when it was less than 5 %. In the present work, FOM was found less than 3 %, which confirms the good agreement between theoretically generated and

experimentally recorded glow curves. The values of trap depth and frequency factor were estimated by CGCD method and summarized in Table 3.

3.6.4. Glow curve shape method

The Chen, Grossweiner and Luschik methods were utilized to estimate the kinetic parameters described elsewhere [54]. The deconvoluted glow curves of SO@STD NPs with coat III irradiated with 8 KGy was shown in Fig.10 (b). The asymmetric glow curves decomposed into symmetrical curves at different positions. The kinetic parameters, such as activation energy, form factor, and frequency factor were estimated. Geometric form factor (μ_g) was determined by using the relation [55]:

$$\mu_g = \frac{T_2 - T_m}{T_2 - T_1} \quad \text{---------- (11)}$$

where, T_m; temperature corresponds to maximum TL intensity, T_1 and T_2; temperatures corresponding to half of maximum TL intensities on the either side. Further, Chen method was used to determine the activation energy using the following equations;

$$E = \frac{2kT_m^2}{\delta} \quad \text{---------- (12)}$$

$$E_\alpha = c_\alpha\left(\frac{kT^2{}_m}{\alpha}\right) - b_\alpha\left(2kT_m\right) \quad \text{---------- (13)}$$

$$E = \frac{2kT_m^2}{\tau}\left(1-3\Delta\right) \quad \text{---------- (14)}$$

where, $\alpha = \tau, \delta, \omega$ with $\tau = T_m - T_1$, $\delta = T_2 - T_m$, $\omega = T_2 - T_1$

$C_\tau = 1.51 + 3.0\left(\mu_g - 0.42\right)$, $b_\tau = 1.58 + 4.2\left(\mu_g - 0.42\right)$

$C_\delta = 0.976 + 7.3\left(\mu_g - 0.42\right)$, $b_\delta = 0$, $C_\omega = 2.52 + 10.2\left(\mu_g - 0.42\right)$, $b_\omega = 1$

$$\Delta_m = \frac{2kT_m}{E} \quad \text{---------- (15)}$$

The trap depth (E) was estimated by using the Grossweiner (16) and Luschik (17) equations:

$$E_\gamma = C_\gamma \frac{KT_m T_1}{\gamma} \text{ ------- (16)}$$

$$E_\gamma = C_\gamma \frac{KT^2{}_m}{\gamma} \text{ ------- (17)}$$

In addition, frequency factor was calculated using the following equation;

$$\frac{\beta E}{kT_m^2} = s \exp\left(\frac{-E}{kT_m}\right)\left[1+(b-1)\Delta_m\right] \quad \text{---------- (18)}$$

where β; linear heating rate, b ; order of kinetics.

The kinetic parameters were estimated and listed in Tables 4, 5 and 6. We know that the order of kinetics lies in the range 0.42 - 0.52, order of kinetics was 1 if μ_g was near to 0.42 and 2 if μ_g was near to 0.52. The trap depth of the deconvoluted peaks was obtained in between the depths 0.48 and 0.98 eV.

3.6.5. Fading and Reproducibility

In order to check the TL stability of the phosphor with time, the samples were stored in dark for different time periods after γ-irradiation and then TL studies were performed. The Fig.10 (c) shows that only 20 % fading was observed for the SiO_2 covered phosphors, not with standing for 30 days of storage periods. It can be clearly seen that the glow peak of SO@STD NPs fades, only for the first 15 days of storage after that insignificant fading was detected beyond this storage period. The present phosphor system exhibit 20 % fading after 30 days of storage, which was considered to be good enough for dosimetric applications [56].

Reproducibility was a vital factor which connotes the viable use of samples in dosimetry [57]. A phosphor was thought to be great if the affectability of the sample stays unaltered after a few redundancies of exposures and readouts. The SO@STD NPs were tried for their reusability. Fig. 10 (d) represents the results after four repeated cycles of annealing-irradiation-readout. The maximum TL intensity varies slightly during the four cycles which

obviously shows that SO@STD NPs can be reused a several times to quantify the ingested measure of radiation in radiation rich territories.

4. Application of the SO@STD NPs for LFPs visualization

In order to determine the efficiency of the prepared NPs for the visualization of LFPs, control experiments were performed using conventional powders (TiO_2 and Fe_2O_3). Fig.11 depicts the photographed images of FPs visualized using the prepared SO@STD NPs and commercially available powders. The obtained results evident that the optimized NPs was most suitable for visualization of the LFPs, revealing explicit, specific ridge characteristics, namely core, bifurcation, ridge ending, bridge, scars, etc. which were most necessitate for the individualization during the forensic investigation. However, the LFPs visualized by staining the Fe_2O_3 and TiO_2 powders, could not reveal more ridge details due to their micron size. Generally, the efficiency of the visualization of LFPs was mainly depends on the chemical compositions of the powders. To achieve better adhesion, the chemical groups present in the powder well react with the LFPs secretions by hydrophobic or electrostatic interactions. In addition, either the endogenous and exogenous sources were the main root cause for the complex chemical constituents present in the LFPs [58]. In the present work, the LFPs were composed of various oily compounds and sweat residues. The prepared NPs with SiO_2 functional group on the surface will readily undergo an electrostatic interaction with the LFPs constituents, leading to highly efficient and better quality FPs images.

To determine the selectivity of the prepared samples to visualization of LFPs, a series of experiments were performed using STD and SO@STD with the coat I-III on the aluminum foil surfaces Fig.12 (a-d). Well-defined ridge structures were clearly revealed in SiO_2 coated NPs stained FPs. Hence, the SO@STD NPs with coat-III was high enough and hence it explored as a new material for LFPs visualization.

Further, we proceed the evaluation work of the utilization of NPs for the visualization of LFPs on various surfaces, such as a wooden floor, glass slide, meter scale and plastic sheet Fig.12 (e-h). More interestingly, high evidential quality of the images with various ridge details including level I- II can be easily revealed. Hence, the obtained results clearly exhibit that the prepared CSs was adaptable and can be used to visualize LFPs on all surfaces.

Fig.13 shows the various ridge features of LFPs visualized by optimized NPs on glass surface under normal light. It was evident from the figure that, the ridge details, namely whorl, short fork, long fork, eye, ridge end, incipient ridge, line fragment, crossover, specialty, hook, dot and island were clearly revealed. Such obtained ridge features are categorized as first and second level features of LFPs and used for personal identification by forensic investigators using the database matching method. Further, with close investigation of obtaining FPs, it was capable to visualize sweat pores organized on the whole FPs ridge patterns. The revealed sweat pores belong to third level features and also utilized for matching purposes. Interestingly, these second and third level features were not revealed when visualized with the commercially used powders.

The practicality of the prepared NPs for the LFPs visualization was evaluated by conducting several experiments after FPs had been aged for several time periods (Fig.14 (a-c)). Generally, the aged LFPs undergo many physical or chemical phenomena, namely evaporation, oxidation, absorption or adsorption, etc. [59]. These phenomena can limit the adhesion efficiency between the prepared powder and LFPs constituents. It was evident from the figure that, the visualization sensitivity gradually diminished with extended aging of the LFPs, due to slow evaporation of the constituents of the LFPs (Fig.14 (a-c)). The obtained results signifying that the sensitivity was high enough for aged LFPs [60]. The effect of temperature on the visualization of LFPs was investigated by treating various temperatures (50,

75, 100 and 150 °C). The obtained result clearly evident that the visualized LFPs were more thermally stable for various temperatures Fig.14 (d-f).

Aforementioned results clearly suggest that, the prepared NPs were successfully explored to visualize LFPs on various surfaces. The developed FPs display high clarity and efficient ridge details as well as sweat pores, which enables the identification of individuals. The chemical constituent's detection present in the sweat pores has yet to be established [61]. Therefore, the present work opens a new possibility of use of prepared NPs for visualization of LFPs in advanced forensic investigations.

5. Conclusions

In summary, we have successfully synthesized SiO_2 coated STD NPs and studied their optical properties to understand the role of the surface effects. The 2 - fold enhancement in the PL intensity was observed in thick coated samples as compared to un-coated ones, which may due to passivation of surface states and reduced surface defects of the NPs after coatings. The photometric properties of all the prepared NPs suggested that CIE coordinates were located in the pure white region with high color purity (~ 88 %). The TL intensity at 200 ^{o}C increases linearly up to 4 kGy and it follows sub-linear up to 7 kGy and thereafter it saturates. The kinetic parameters were estimated by various glow curve analysis methods show a close agreement. The SO@STD NPs exhibit high sensitivity and low fading (20 %) with good reproducibility (up to four cycles) behavior. Finally, the optimized SO@STD NPs was explored as a labelling agent for the visualization of LFPs, due to its high adhering efficiency with fat, amino acids and proteins present in the LFPs, revealing well-defined ridge micro-structures, namely whorl, short fork, long fork, eye, ridge end, incipient ridge, line fragment, cross-over, specialty, hook, dot and island. In addition, the sweat pores organized on the whole FPs ridge patterns were also revealed which were utilized for matching purposes. Interestingly, these second and third level features were not revealed when visualized with the commercially used powders. Hence, our results demonstrating that the flawed method and used NPs can be used for visualization of LFPs with high clarity, sensitivity, selectivity and low background hindrance on various surfaces. The aforementioned results clearly suggest that SO@STD NPs can be quite useful in radiation dosimetry, WLEDs and forensic applications.

References

1. A. Sandhyarani, M.K. Kokila, G.P. Darshan, R.B. Basavaraj, B. Daruka Prasad, S.C. Sharma, T.K.S. Lakshmi, H. Nagabhushana, Versatile core-shell SiO_2@$SrTiO_3$:Eu^{3+}, Li^+ nanopowders as fluorescent label for the visualization of latent fingerprints and anti-counterfeiting applications, Chem. Eng. J. 327 (2017) 1135-1150.
2. K.N. Venkatachalaiah, H. Nagabhushana, G.P. Darshan, R.B. Basavaraj, B. Daruka Prasad, Novel and highly efficient red luminescent sensor based SiO_2@Y_2O_3:Eu^{3+}, M^+ (M^+ = Li, Na, K) composite core–shell fluorescent markers for latent fingerprint recognition, security ink and solid state lightning applications, Sens. Actuators, B. 251 (2017) 310-325.
3. C.E. Secu, M. Secu, M. Cernea, Synthesis and up-conversion luminescence properties of BaFBr-Er^{3+}@SiO_2 core/shell heterostructures, J. Lumin. 188 (2017) 96-100.
4. M. Secu, M. Cernea, C.E. Secu, B.S. Vasile, Structural and optical properties of fluorescent BaFBr-Eu^{2+}@SiO_2 core/shell phosphor heterostructure, Mater. Chem. Phys. 151 (2015) 81-86.
5. L. Liu, H. Xiao, X. An, Y. Zhang, R. Qin, L. Liu, D. Zhang, R. Sun, L. Chen, Synthesis and photoluminescence properties of core–shell structured YVO_4:Eu^{3+}@SiO_2 nanocomposites, Chem. Phys. Lett. 619 (2015) 169-173.
6. Chenning Zhang, Tetsuo Uchikoshi, Rong-Jun Xie, Lihong Liu, Yoshio Sakka, Naoto Hirosaki, Photoluminescence efficiency significantly enhanced by surface modification of SiO_2 coating on β-sialon:Eu^{2+} phosphor particle, , J Alloys Compd. 741 (2018) 454-458.
7. Jie Lu MD, Zongxi Li BS, Jeffrey I. Zink, FuyuhikoTamanoi, In vivo tumor suppression efficacy of mesoporous silica nanoparticles-based drug-delivery system: enhanced efficacy by folate modification, Nanomedicine: Nanotechnology, Biology and Medicine, 8 (2012) 212-220.
8. K. M. Choi, H. S. Kil, Y. S. Lee, D. Y. Lim, S. B. Cho, B. W. Lee, Preparation and luminescence properties of $SrTiO_3$:Pr^{3+}, Al^{3+} phosphor from the glycolate method, J Lumin, 131 (2011) 894-899.
9. Lucas Angelini Deltreggia, Maria Inês Basso Bernardi, Alexandre Mesquita, Influence of La substitution on local structural and photoluminescence properties of $SrTiO_3$:Pr phosphor, Scr. Mater. 157 (2018) 15–18.
10. B. Mari, K.C. Singh, Paula Cembrero-Coca, Ishwar Singh, Devender Singh, Subhash Chand, Red emitting $MTiO_3$ (M = Ca or Sr) phosphors doped with Eu^{3+} or Pr^{3+} with some cations as co-dopants, Displays. 34 (2013) 346–351.
11. P. Jayabal, V. Sasirekha, J. Mayandi, K. Jeganathan, V. Ramakrishnan, A facile hydrothermal synthesis of $SrTiO_3$ for dye sensitized solar cell application, J. Alloys Compd. 586 (2014) 456–461.
12. R.B. Basavaraj, H. Nagabhushana, B. Daruka Prasad, G.R. Vijayakumar, Zinc silicates with tunable morphology by surfactant assisted sonochemical route suitable for NUV excitable white light emitting diodes, Ultrason. Sonochem. 34 (2017) 700–712.
13. R.B. Basavaraj, H. Nagabhushana, G.P. Darshan, B. Daruka Prasad, S.C. Sharma, K.N. Venkatachalaiah, Ultrasound assisted rare earth doped Wollastonite nanopowders: Labeling agent for imaging eccrine latent fingerprints and cheiloscopy applications, J. Ind. Eng. Chem. 51 (2017) 90-105.
14. M. Dhanalakshmi, H. Nagabhushana, G.P. Darshan, R.B. Basavaraj, B. Daruka Prasad, Sonochemically assisted hollow/solid $BaTiO_3$:Dy^{3+} microspheres and their applications in effective detection of latent fingerprints and lip prints, J. Sci.: Adv. Mater. Devices. 2 (2017) 22-23.

15. Shiuh-Tsuen Huang, Wenlian William Lee, Jia-Lin Chang, Wu-Sheng Huang, Shang-YiChou, Chiing-Chang Chen, Hydrothermal synthesis of $SrTiO_3$ nanocubes: Characterization, photocatalytic activities, and degradation pathway, J. Taiwan Inst. Chem. Eng. 45 (2014) 1927-1936.
16. Takeshi Kimijima, Kiyoshi Kanie, Masafumi Nakaya, Atsushi Muramatsu, Solvothermal synthesis of $SrTiO_3$ nanoparticles precisely controlled in surface crystal planes and their photocatalytic activity, Appl. Catal., B. 144 (2014) 462-467.
17. Hongtao Cui, Marcos Zayat, David Levy, Controlled homogeneity of the precursor gel in the synthesis of $SrTiO_3$ nanoparticles by an epoxide assisted sol–gel route, J. Non-Cryst. Solids. 353 (2007) 1011-1016.
18. R.B. Basavaraj, H. Nagabhushana, G.P. Darshan, B. Daruka Prasad, M. Rahul, S.C. Sharma, R. Sudaramani, K.V. Archana, Red and green emitting CTAB assisted $CdSiO_3$: Tb^{3+}/Eu^{3+} nanopowders as fluorescent labeling agents useful for forensic and display applications, Dyes Pig. 147 (2017) 364-377.
19. C. Suresh, H. Nagabhushana, G.P. Darshan, R.B. Basavaraj, B. Daruka Prasad, S.C. Sharma, M.K. Sateesh, J.P. Shabaaz Begum, Lanthanum oxyfluoride nanostructures prepared by modified sonochemical method and their use in the fields of optoelectronics and biotechnology, Arabian J. Chem. 11 (2018) 196-213.
20. N.H. Deepthi, G.P. Darshan, R.B. Basavaraj, B. Daruka Prasad, H. Nagabhushana, Large-scale controlled bio-inspired fabrication of 3D CeO_2:Eu^{3+} hierarchical structures for evaluation of highly sensitive visualization of latent fingerprints, Sens. Actuators, B. 255 (2018) 3127-3147.
21. S. Roomi, S. Ali, H. Ahmad, K. Hayat, S. Zulfiqar, Y. Iqbal, Development of a new rare-earth (Dy^{3+})-based thermoluminescent dosimeter, J. Lumin. 196 (2018) 373-378.
22. M. Venkataravanappa, H. Nagabhushana, G.P. Darshan, S.C. Sharma, K.V. Archana, R.B. Basavaraj, B. Daruka Prasad, Facile ultrasound route for the fabrication of green emitting Ba_2SiO_4:Eu^{2+} nanophosphors for display and dosimetric applications, Mat. Res. Bull. 97 (2018) 281-292.
23. N. Bajpai, S.A. Khan, R.S. Kher, N. Bramhe, S.J. Dhoble, A. Tiwari, Thermoluminescence investigation of sol–gel derived and γ-irradiated SnO_2:Eu^{3+} nanoparticles, J. Lumin. 145 (2014) 940-943.
24. R.G. Nair, K. Madhukumar, C.M.K. Nair, S. Jayasudha, V.M. Anandakumar, T.S. Elias, Manoj Komath, Thermoluminescence studies of $CaSO_4$:Dy, P, Si phosphor under X-ray irradiation, Ceram. Int. 44 (2018) 3492-3496.
25. D.J. Daniel, H.J. Kim, S. Kim, Synthesis, X-ray, and thermoluminescence properties of $Li_3K_3Y_7(BO_3)_9$, Ceram. Int. 44 (2018) 8184-8189.
26. M. Chowdhury, S.K. Sharma, S.P. Lochab, Thermoluminescence glow curve analysis of γ-irradiated Eu^{3+} doped SnO_2 composites, Ceram. Int. 42 (2016) 5472-5478.
27. E. Padmini, K. Ramachandran, M. Muralidharan, Structural, optical, magnetic and dielectric properties of Dy-doped $SrTiO_3$ nano ceramics, J. Mater. Sci.: Mater. Electron. https://doi.org/10.1007/s10854-018-9804-7.
28. C. Suresh, H. Nagabhushana, R.B. Basavaraj, G.P. Darshan, D. Kavyashree, B. Daruka Prasad, S.C. Sharma, R. Vanithamani, SiO_2@LaOF:Eu^{3+} core-shell functional nanomaterials for sensitive visualization of latent fingerprints and WLED applications, J. Colloid and Interface Sci. 518 (2018) 200-215.
29. Dhanalakshmi Muniswamy, Hanumanthappa Nagabhushana, R.B. Basavaraj, Giriyapura Prabhukumar Darshan, Daruka Prasad B, Surfactant-Assisted $BaTiO_3$:Eu^{3+}@SiO_2 Core–Shell Superstructures Obtained by Ultrasonication Method: Dormant Fingerprint Visualization and Red Component of White Light-Emitting Diode Applications, ACS Sustainable Chem. Eng. 6 (2018) 5214–5226.

30. Young-Jae Kim, Hak-Sung Jung, Joohyun Lim, Seung-Jin Ryu, Jin-Kyu Lee, Rapid Imaging of Latent Fingerprints Using Biocompatible Fluorescent Silica Nanoparticles, Langmuir, 32 (2016) 8077–8083.
31. Wei Huang, Xiaojun Li, Hongfei Wang, Xiaojing Xu, Huan Liu, Guiqiang Wang, Synthesis of Amphiphilic Silica Nanoparticles for Latent Fingerprint Detection, Anal. Lett. 48 (2014) 1524-1535.
32. F. Femila Komahal, H. Nagabhushana, R.B. Basavaraj, G.P. Darshan, B. Daruka Prasad, S.C. Sharma, D. Kavyashree, Design of Bi-functional composite core–shell SiO_2@$ZnAl_2O_4$:Eu^{3+} array as a fluorescent sensors for selective and sensitive latent fingerprints visualization protocol, Adv. Powder Technol. 29 (2018) 1991-2002.
33. Zhennan Shi, Chen Xu, Peng Lu, Lu Fan, Yana Liu, Yingxi Wang, Li Liu, Ling Li, Preparation and the adsorption ability of thiolated magnetic core-shell Fe_3O_4@SiO_2@C-SH for removing Hg^{2+} in water solution, Mater. Lett. 225 (2018) 130-133.
34. R.B. Basavaraj, H. Nagabhushana, B. Daruka Prasad, S.C. Sharma, K.N. Venkatachalaiah, Mimosa pudica mediated praseodymium substituted calcium silicate nanostructures for white LED application, J Alloys Compd. 690 (2017) 730-740.
35. M. Dhanalakshmi, H. Nagabhushana, G.P. Darshan, R.B. Basavaraj, B. Daruka Prasad, Sonochemically assisted hollow/solid $BaTiO_3$:Dy^{3+} microspheres and their applications in effective detection of latent fingerprints and lip prints, J. Sci.: Adv. Mater. Devices. 2 (2017) 22-33.
36. C. Suresh, H. Nagabhushana, G.P. Darshan, R.B. Basavaraj, B. Daruka Prasad, S.C. Sharma, M.K. Sateesh, J.P. Shabaaz Begum, Lanthanum oxyfluoride nanostructures prepared by modified sonochemical method and their use in the fields of optoelectronics and biotechnology, Arabian J. Chem. 11 (2018) 196-213.
37. L.F. da Silva, W. Avansi, J. Andres, C. Ribeiro, M.L. Moreira, E. Longo, V.R. Mastelaro, Long-range and short-range structures of cube-like shape SrTiO3 powders: microwave-assisted hydrothermal synthesis and photocatalytic activity, Phys. Chem. Chem. Phys. 15 (2013) 12386–12393.
38. F. Carrillo Romo, A. García Murillo, D. López Torres, N. Cayetano Castro, V.H. Romero, E. de la Rosa, V. Garibay Febles, M. García Hernández, Structural and luminescence characterization of silica coated Y_2O_3:Eu^{3+} nanopowders, Opt. Mater. 32 (2010) 1471–1479.
39. Guixia Liu, Guangyan Hong, Xiangting Dong, Jinxian Wang, Silica-coated Y_2O_3:Eu nanoparticles and their luminescence properties, J. Lumin. 126 (2007) 702–706.
40. Tong Liu, Wen Xu, Xue Bai, Hongwei Song, Tunable silica shell and its modification on photoluminescent properties of Y_2O_3:Eu^{3+}@SiO_2 nanocomposites, J. Appl. Phys. 111 (2012) 064312.
41. Meitram Niraj Luwang, Raghumani Singh Ningthoujam, Sri Krishna Srivastava, Rajesh Kumar Vatsa, Preparation of white light emitting YVO_4: Ln^{3+} and silica-coated YVO_4:Ln^{3+} (Ln^{3+} = Eu^{3+}, Dy^{3+}, Tm^{3+}) nanoparticles by CTAB/n-butanol/hexane/water microemulsion route: Energy transfer and site symmetry studies, J. Mater. Chem., 21 (2011) 5326–5337.
42. Guixia Liu, Guangyan Hong, Duoxian Sun, Coating Gd_2O_3:Eu phosphors with silica by solid-state reaction at room temperature, Powder Technol. 145 (2004) 149– 153.
43. H. Wang, M. Yua, C.K. Lin, J. Lin, Core–shell structured SiO_2@YVO_4:Dy^{3+}/Sm^{3+} phosphor particles: Sol–gel preparation and characterization, J. Colloid Interface Sci.300 (2006) 176–182.
44. Young Kyu Jeong, Hyug-Jong Kim, Hee Gyu Kim, Byung-Ho Choi, Luminescent properties of $BaMgAl_{10}O_{17}$:Eu^{2+} blue phosphor grown with SiO_2 using atomic layer deposition, Curr. Appl Phys. 9 (2009) S249–S251.

45. Guangzhi Li, Zhenling Wang, Min Yu, Zewei Quan, Jun Lin, Fabrication and optical properties of core–shell structured spherical SiO_2@$GdVO_4$:Eu^{3+} phosphors via sol–gel process, J. Solid State Chem. 179 (2006) 2698–2706.
46. S.H. Sohn, J.H. Lee, S.M. Lee, Effects of the Surface Coating of $BaMgAl_{10}O_{17}$:Eu^{2+} Phosphor with SiO_2 Nano-Particles, J. Lumin. 129 (2009) 478–481.
47. Guangzhi Li, Zhenling Wang, Zewei Quan, Chunxia Li, Jun Lin, Growth of Highly Crystalline $CaMoO_4$:Tb^{3+} Phosphor Layers on Spherical SiO_2 Particles via Sol-Gel Process: Structural Characterization and Luminescent Properties, Cryst. Growth Des. 7 (2007) 1797-1802.
48. F.B. Xiong, S.X. Liu, H.F. Lin, X.G. Meng, S.Y. Lian, W.Z. Zhu, A novel white-light-emission phosphor Dy^{3+}-doped $CaLaB_7O_{13}$ under UV excitation, Opt. Laser Technol. 106 (2018) 29-33.
49. Publication CIE No 15.2, Colorimetry, second ed., Central Bureau of the Commission Internationale de L'Eclairage, Vienna, Austria, 1986.
50. M. Venkataravanappa, R.B. Basavaraj, G.P. Darshan, B. Daruka Prasad, S.C. Sharma, P. Hema Prabha, S. Ramani, H. Nagabhushana, Multifunctional Dy (III) doped di-calcium silicate array for boosting display and forensic applications, J. Rare Earths. 36 (2018) 690-702.
51. H.S. Yogananda, R.B. Basavaraj, G.P. Darshan, B. Daruka Prasad, Ramachandra Naik, S.C. Sharma, H. Nagabhushana, New design of highly sensitive and selective MoO_3:Eu^{3+} micro-rods: Probing of latent fingerprints visualization and anti-counterfeiting applications, J. Colloid Interface Sci. 528 (2018) 443-456.
52. G.M. Hassan, E. Aboelezz, A.M. Sadek, M.A. Sharaf, Glow curve deconvolution of nano barium strontium sulfate and thermoluminescence trap centers behavior with gamma doses, J. Lumin. 179 (2016) 616-621.
53. S. Balci-Yegen, M. Yüksel, N. Kucuk, Y. Karabulut, M. Ayvacikli, N. Can, M. Topaksu, Thermoluminescence dose and heating rate dependence and kinetic analysis of ZnB_2O_4:$0.05Dy^{3+}$ phosphor, Nucl. Instrum. Methods Phys. Res., Sect. B. 416 (2018) 50-54.
54. M. Chowdary, S.K. Sharma, S.P. Lochab, Gamma ray induced thermoluminescence properties of Eu^{3+} doped SnO_2 phosphor, Mater. Res. Bull. 70 (2015) 584-589.
55. P. Dewangan, D.P. Bisen, N. Brahme, R.K. Tamrakar, K. Upadhyay, S. Sharma, I.P. Sahu, Studies on thermoluminescence properties of alkaline earth silicate phosphors, J. Alloys Compd. 735 (2018) 1383-1388.
56. Jyoti Singh, J. Manam, Fouran Singh, Synthesis and thermoluminescence studies of γ-irradiated Dy^{3+} doped $SrGd_2O_4$ phosphor, Mater. Res. Bull. 94 (2017) 113–121.
57. Raunak Kumar Tamrakar, D.P. Bisen, Kanchan Upadhyay, Change in thermoluminescence behaviour of cubic Gd_2O_3:Yb^{3+} phosphors with successive increase in Yb^{3+} ion concentrations, Radiat. Phys. Chem. 130 (2017) 321–334.
58. You-Hong Chen, Shih-Yu Kuo, Wei-Kai Tsai, Chi-Shiang Ke, Chia-Hsien Liao, Chuan-Pin Chen, Yeng-Tseng Wang, Hsiu-Wei Chen, and Yang-Hsiang Chan, Dual colorimetric and fluorescent imaging of latent fingerprints on both porous and nonporous surfaces with near-infrared fluorescent semiconducting polymer dots. Anal. Chem. 88 (2016)11616–11623. http://dx.doi.org/10.1021/acs.analchem.6b03178.
59. Cheng Y-H, Zhang Y, Chau S-L, Lai SK-M, Tang H-W, Ng K-M. Enhancement of image contrast, stability, and SALDI-MS detection sensitivity for latent fingerprint analysis by tuning the composition of silver-gold nanoalloys. ACS Appl. Mater. Interfaces. 8 (2016) 29668–29675. http://dx.doi.org/10.1021/acsami.6b09668.

60. Cai K, Yang R, Wang Y, Yu X, Liu J. Super-fast detection of latent fingerprints with water soluble CdTe quantum dots. Forensic Sci. Int. 226 (2013) 240–243. http://dx.doi. org/10.1016/j.forsciint.2013.01.035.
61. B. Marappa, M.S. Rudresha, R.B. Basavaraj, G.P. Darshan, B. Daruka Prasad, S.C. Sharma, S. Sivakumari, P. Amudha, H. Nagabhushana, EGCG assisted Y_2O_3:Eu^{3+} nanopowders with 3D micro-architecture assemblies useful for latent finger print recognition and anti-counterfeiting applications, Sens. Actuators, B . 264 (2018) 426-439.

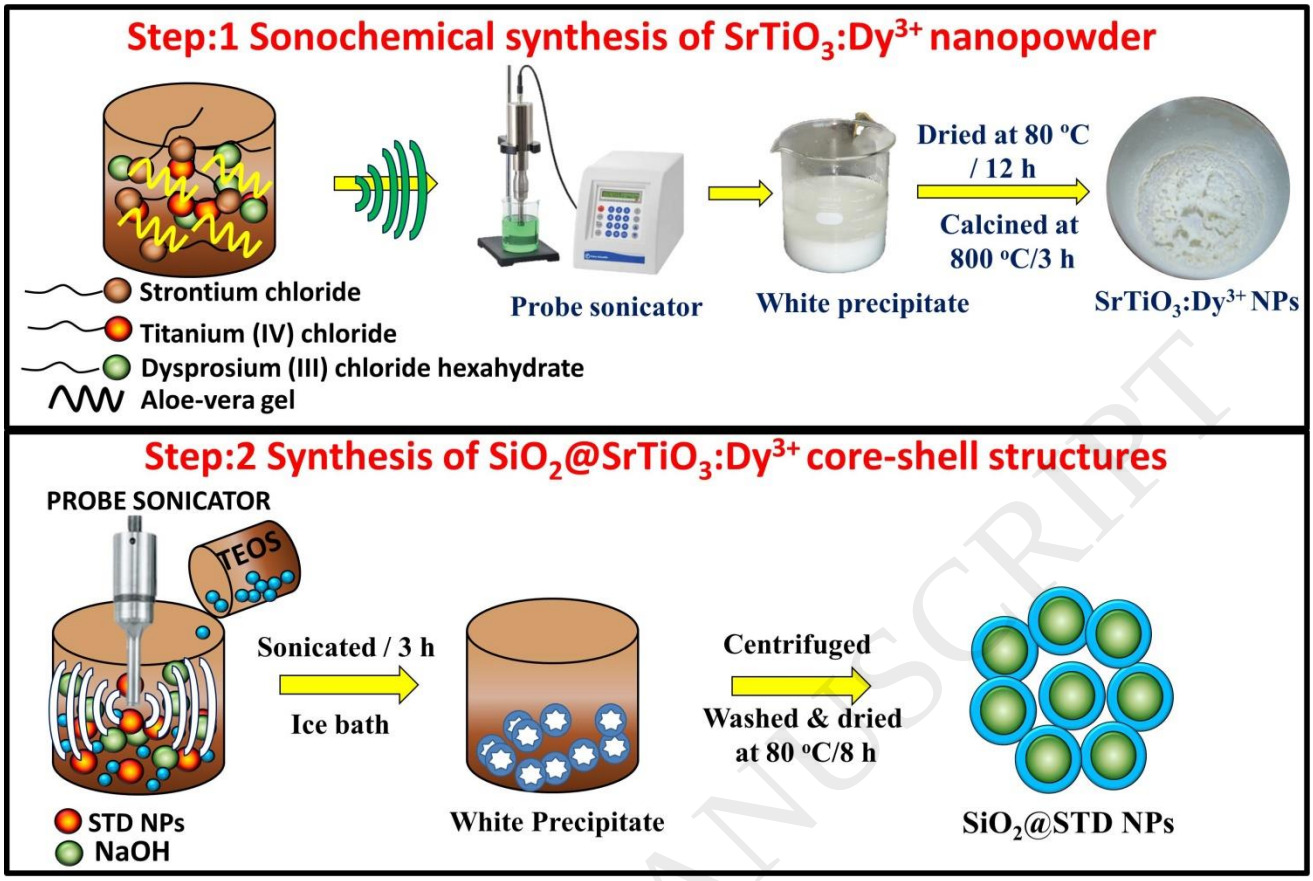

Fig.1. Schematic illustration for the synthesis of STD NPs by ultrasonication route and its surface modification by SiO_2 by Stöber method.

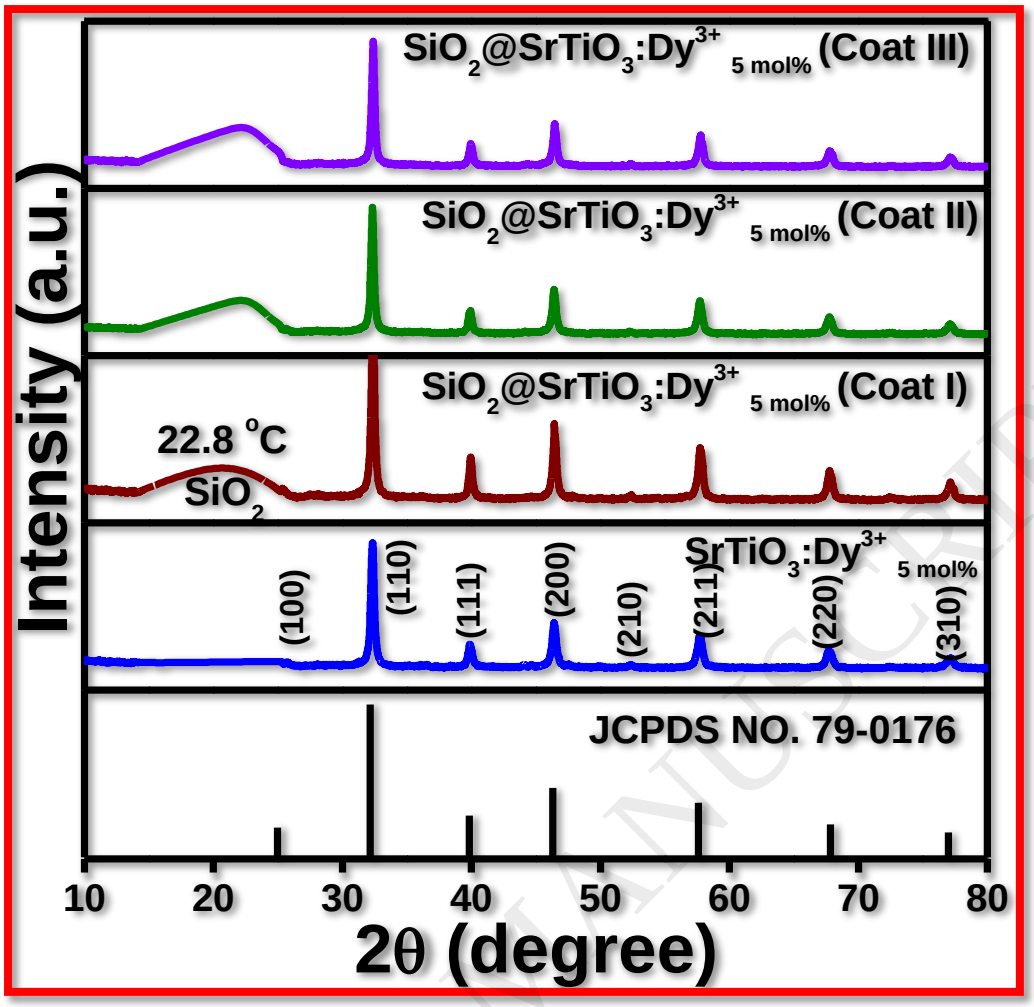

Fig.2. PXRD patterns of STD and SO@STD NPs.

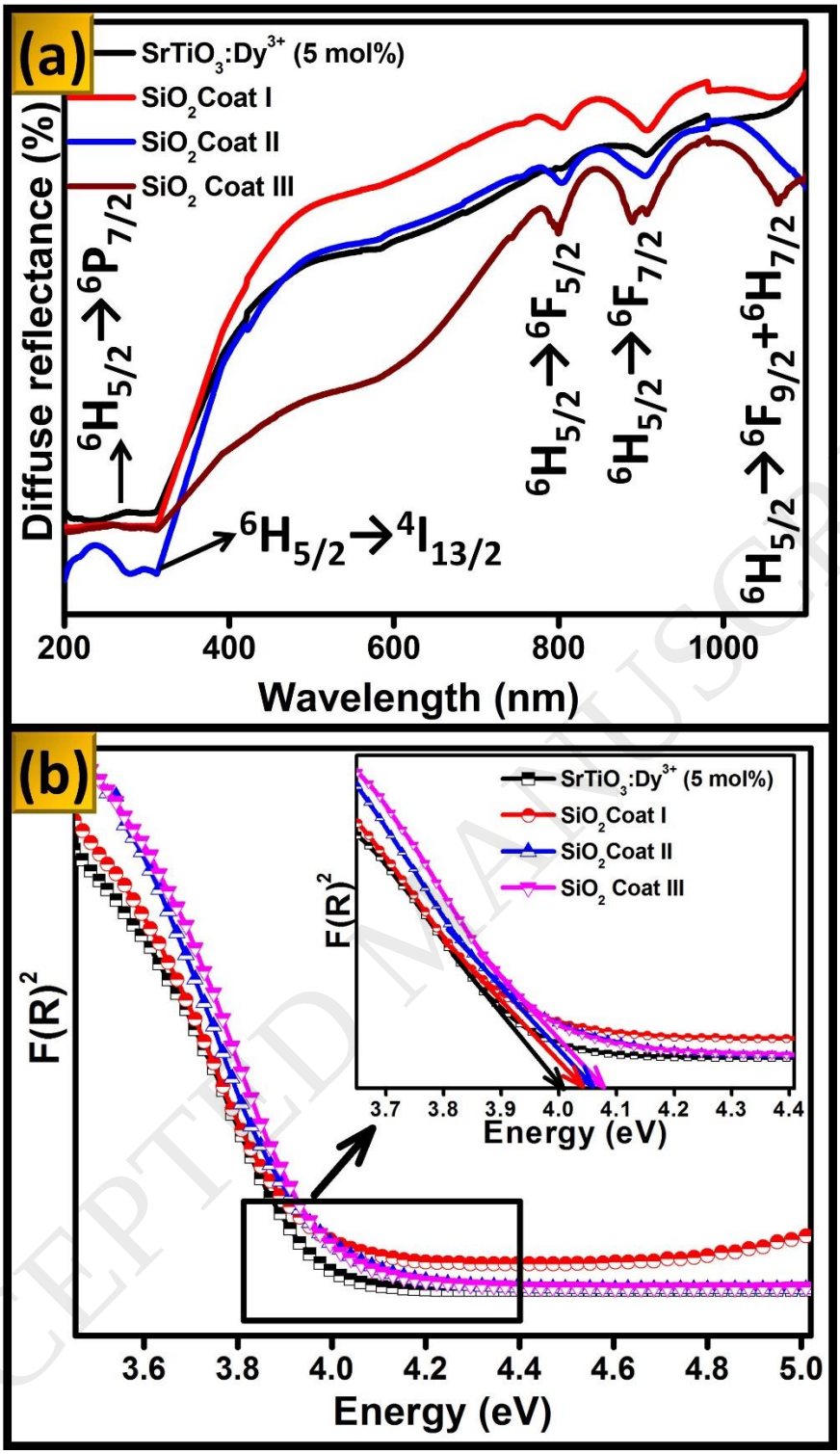

Fig.3 (a) DR spectra and (b) Energy band gap plots of STD and SO@STD NPs.

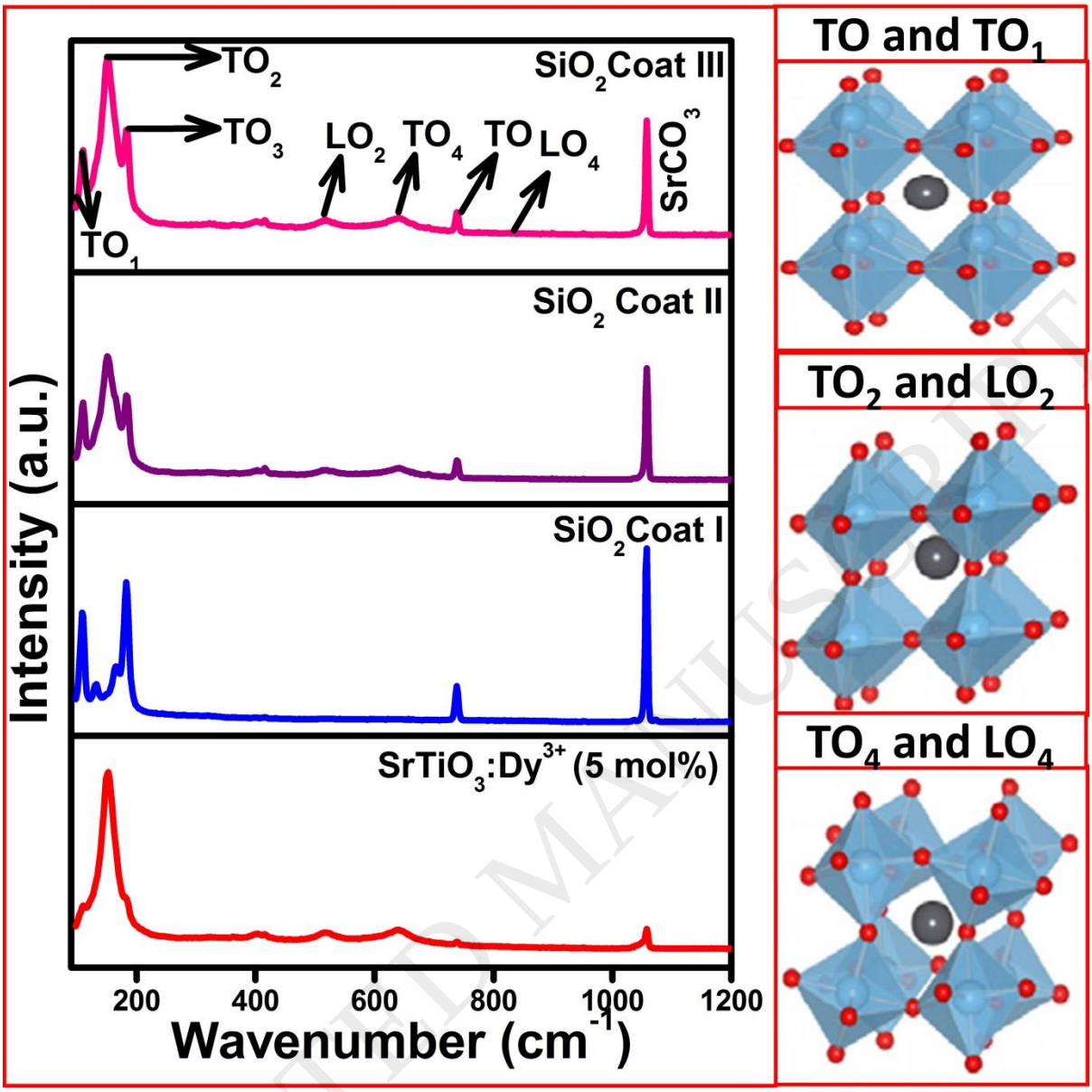

Fig.4. Raman spectra of STD and SO@STD NPs.

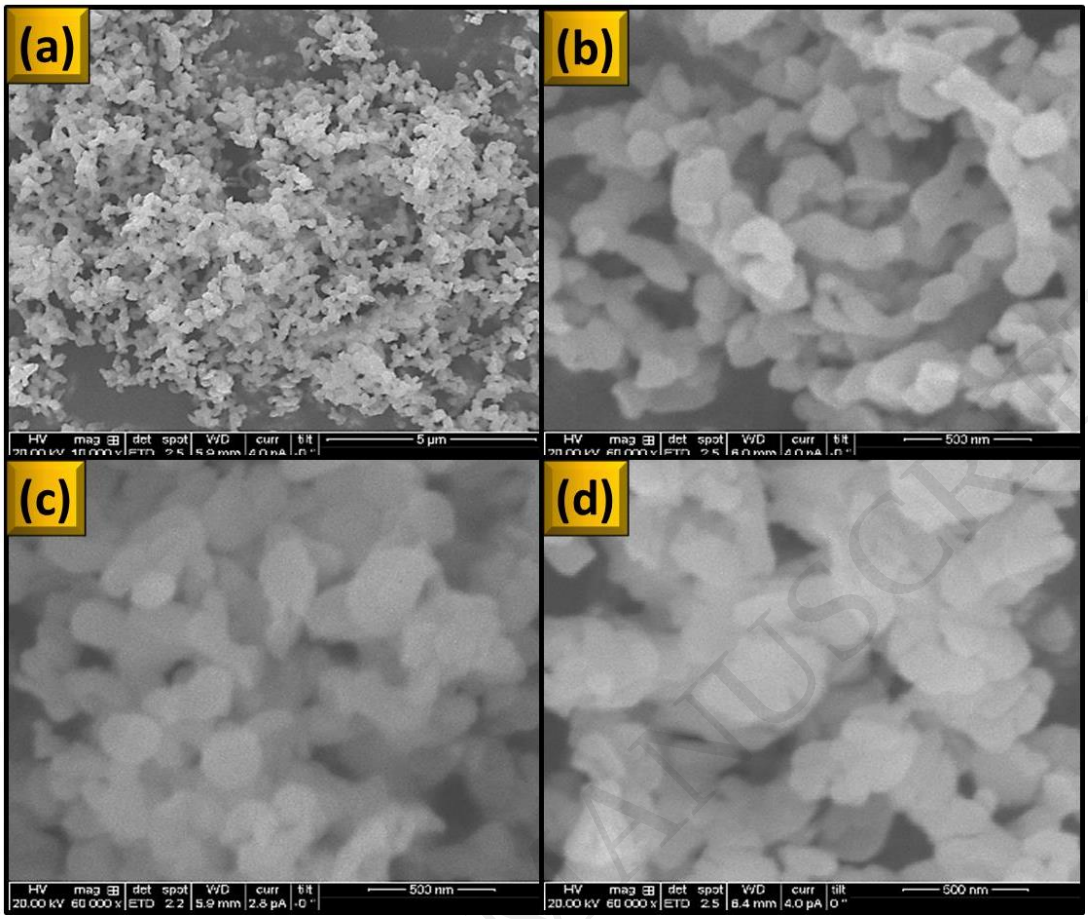

Fig.5. SEM micrographs of (a) STD NPs, (b-d) SO@STD NPs with coat I-III.

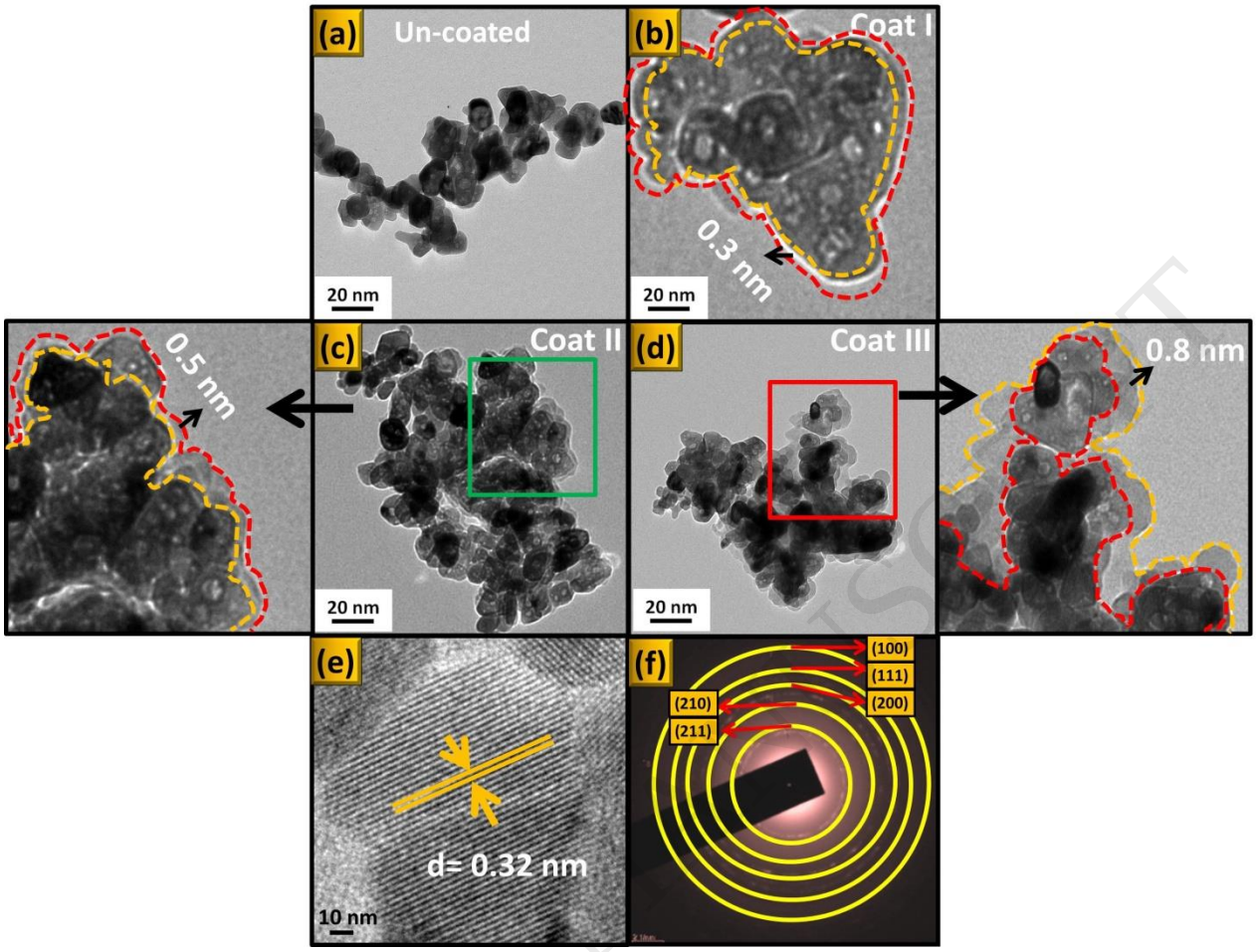

Fig.6 (a-d) TEM images of STD and SO@STD NPs, (e) HRTEM image and (f) SAED patterns of SO@STD NPs with coat III.

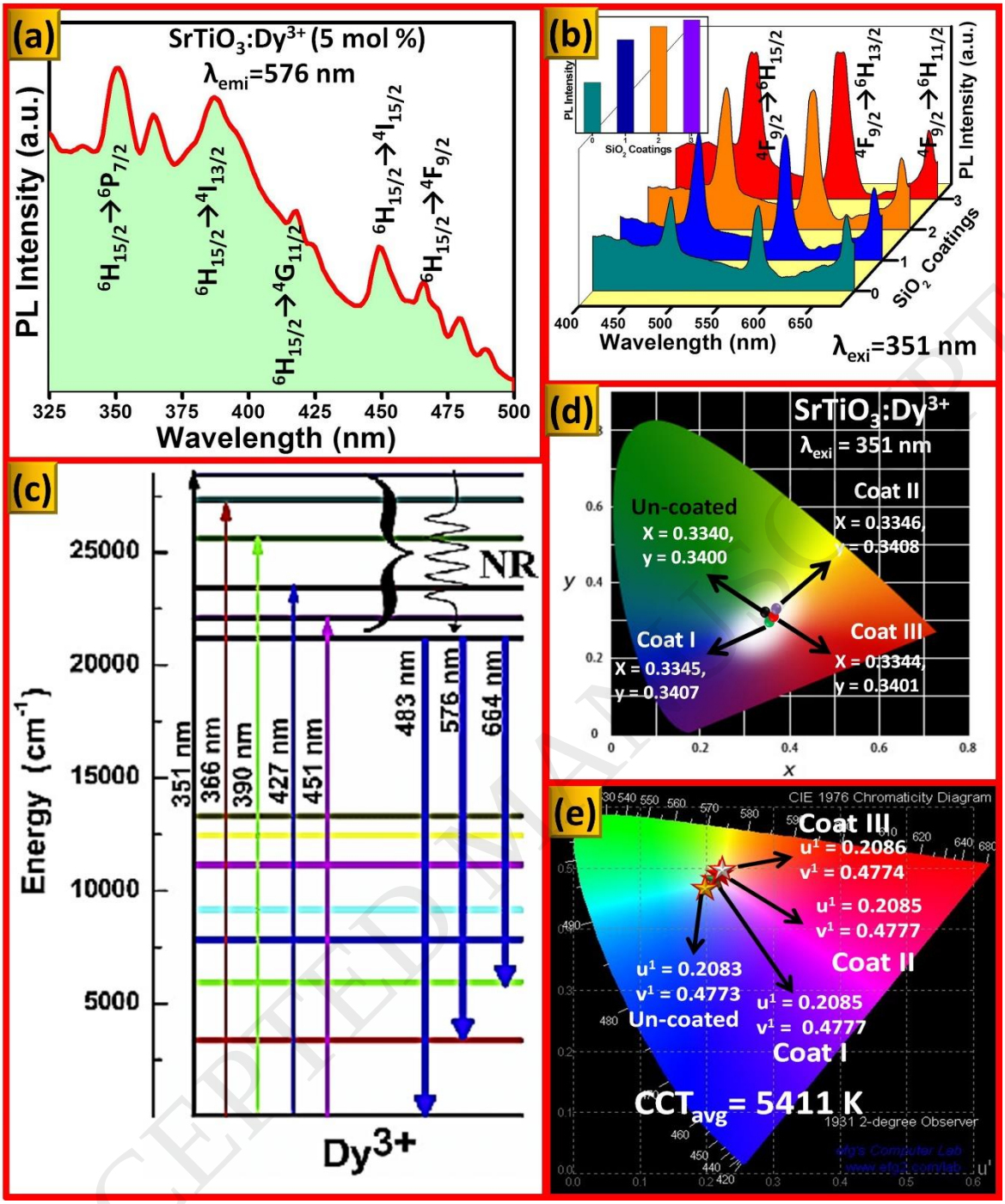

Fig.7 (a) PL excitation spectrum of STD NPs, (b) Emission spectra of STD and SO@STD NPs with coat I-III, (c) energy level diagram of Dy^{3+} ions in $SrTiO_3$ host, (d & e) CIE and CCT diagrams of STD and SO@STD NPs. [Inset of Fig. 7(b): Variation of PL intensity V/S SiO2 coatings].

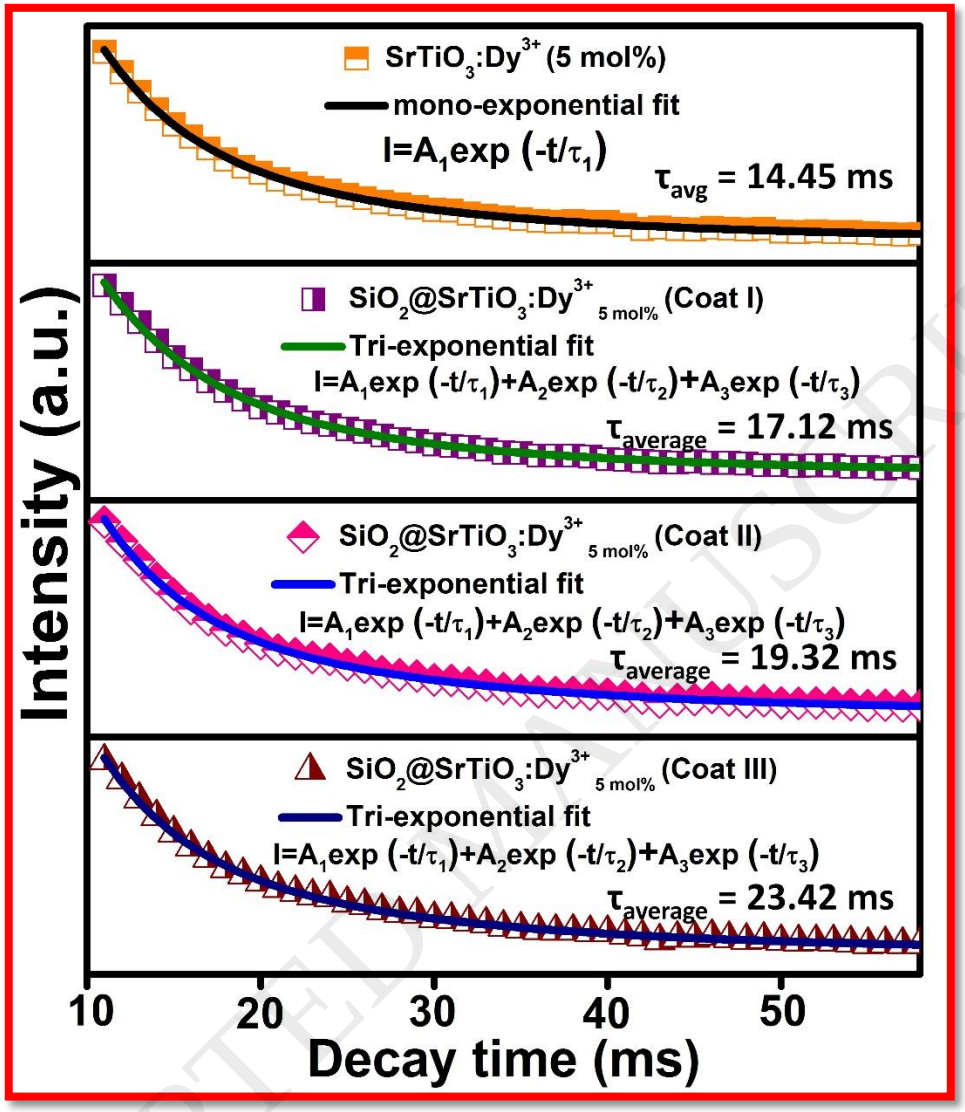

Fig.8. PL decay curves of STD NPs and SO@STD NPs.

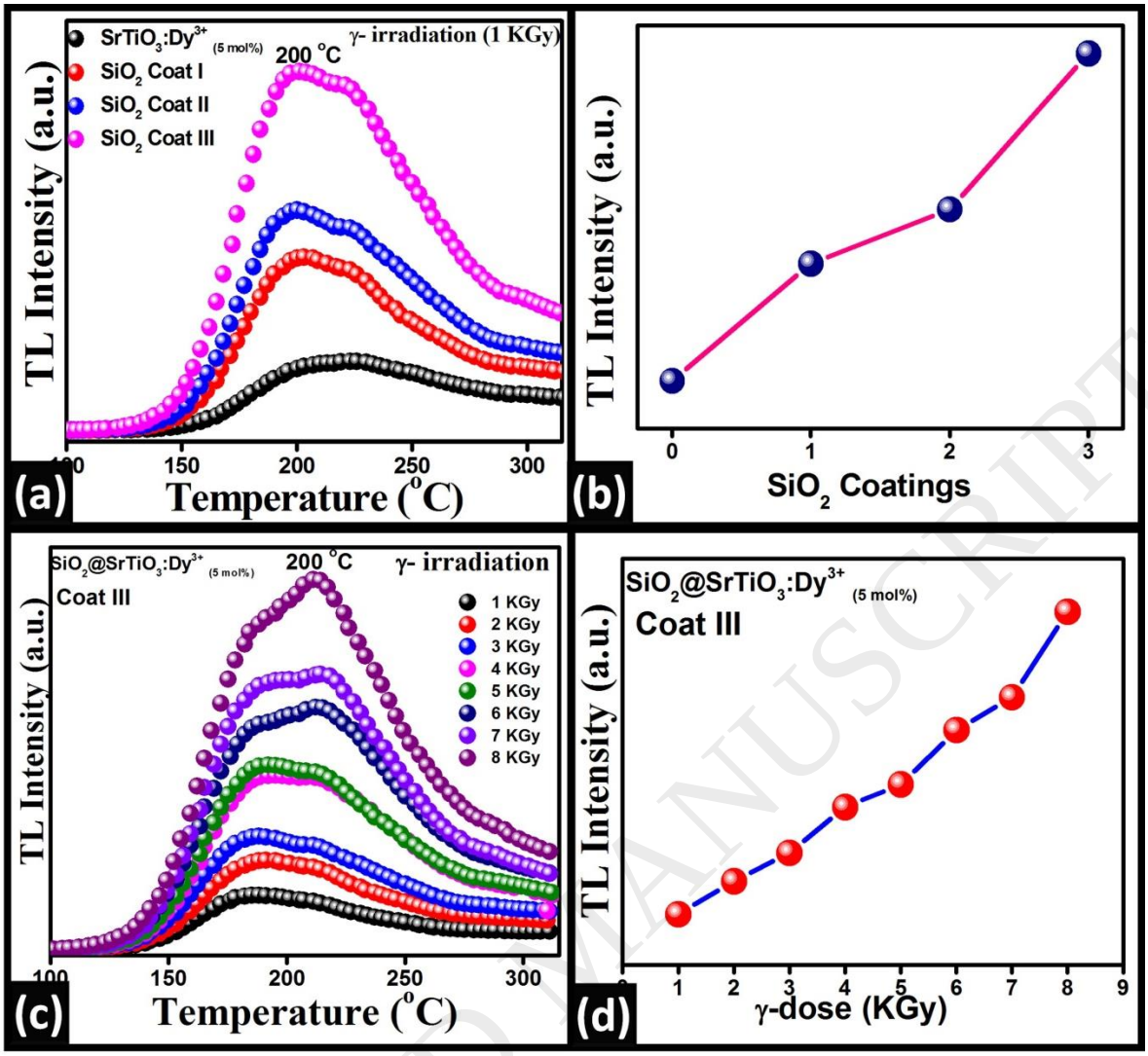

Fig.9 (a) TL glow curves of STD and SO@STD NPs under 1 kGy γ-dose, (b) Variation of TL intensity with SiO_2 coating, (c) TL glow curves of SO@STD NPs coat III under 1-8 kGy γ-dose and (d) variation plot of TL intensity versus γ-dose.

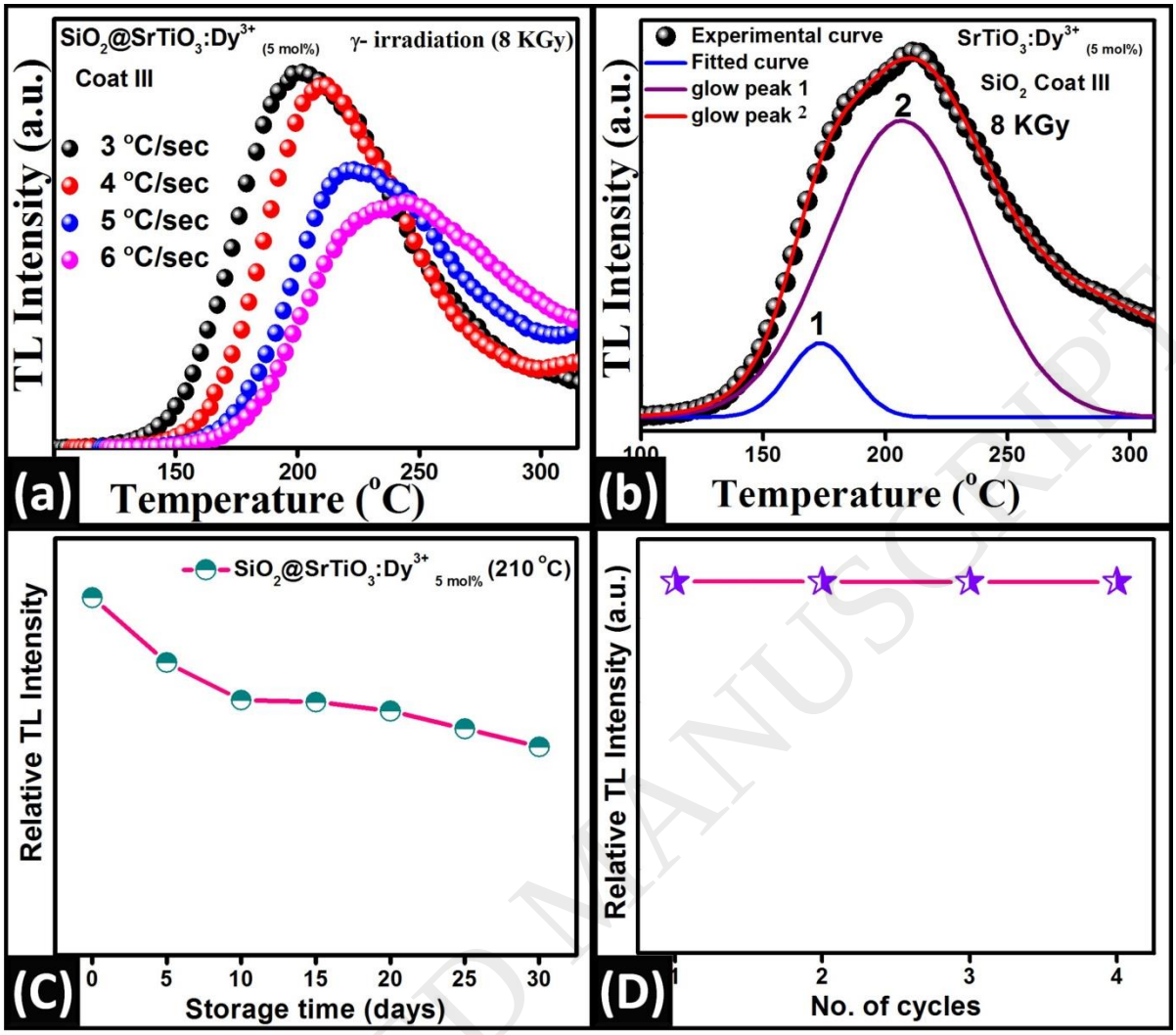

Fig.10 (a) TL glow curves of STD and SO@STD NPs with different heating rates under 8 kGy γ-dose, (b) Experimental and deconvoluted glow peaks of SO@STD NPs under 8 kGy γ-dose, (c) TL fading and (b) Reproducibility characteristics of SO@STD NPs with 8 kGy γ-ray exposition.

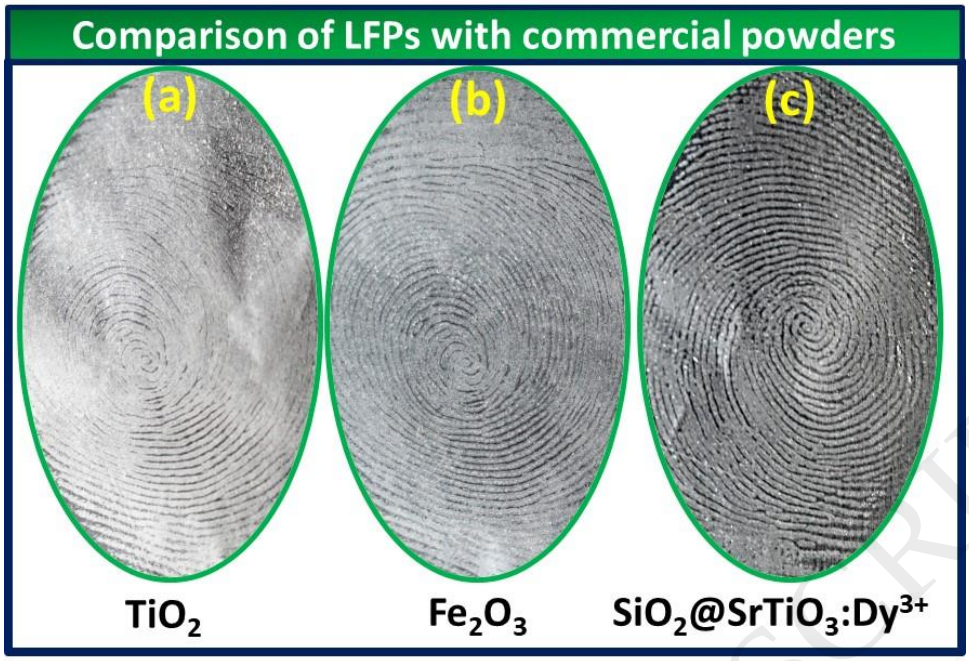

Fig.11. LFPs visualized by staining commercial powders and SO@STD NPs.

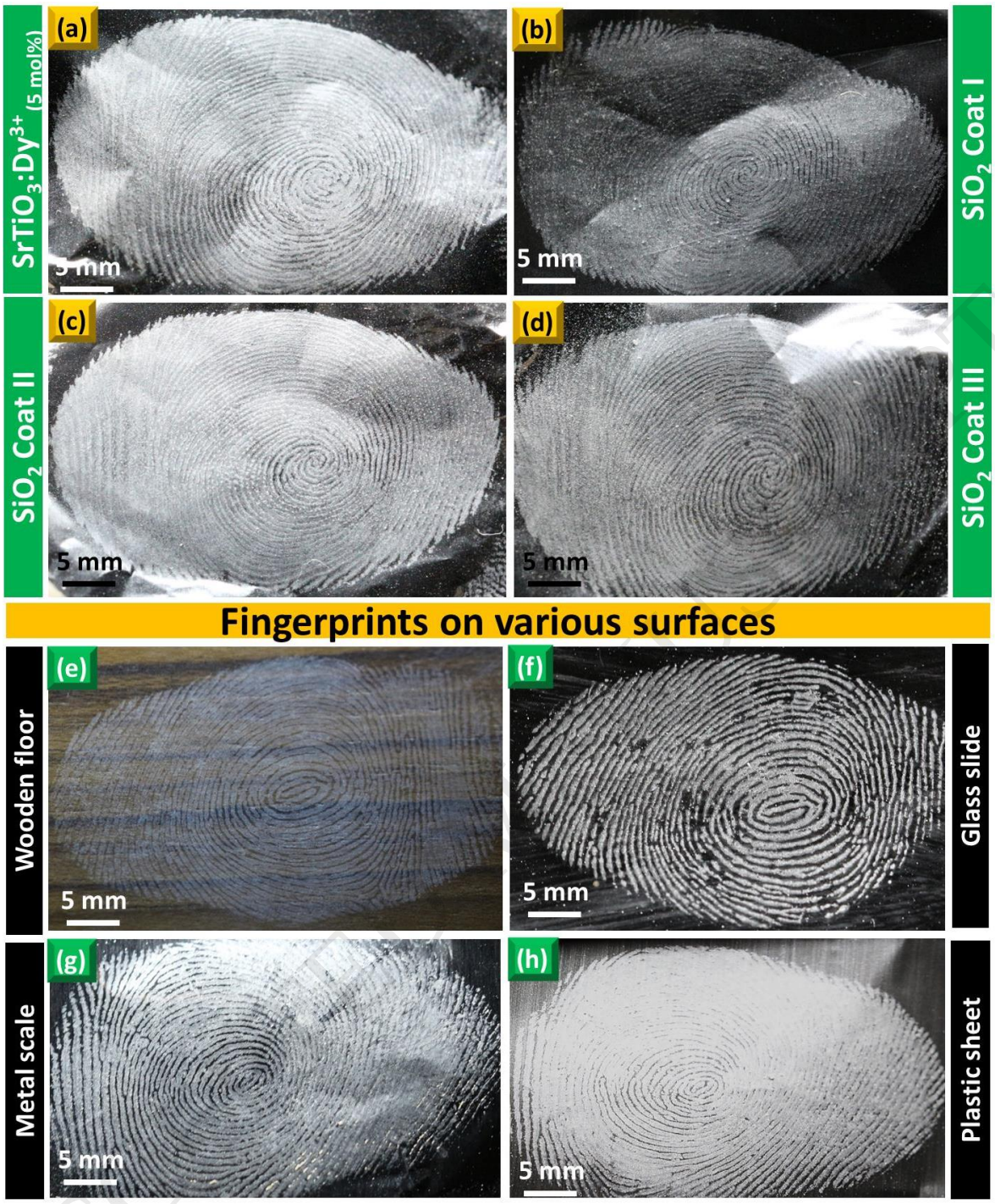

Fig.12. Visualization of LFPs on aluminum foil surface using (a) STD NPs, (b-d) SO@STD NPs with coat I-III, (e-h) LFPs visualized by staining optimized SO@STD NPs with coat III on various surfaces under normal light.

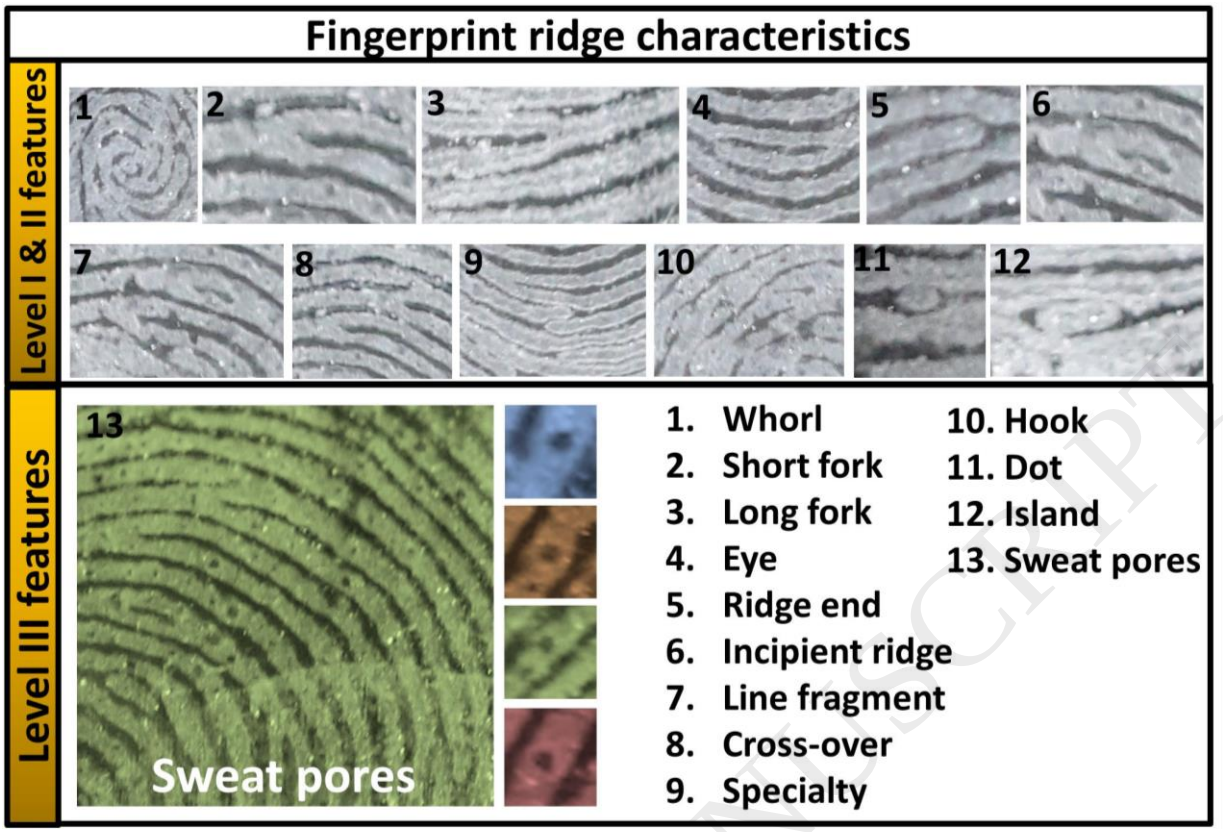

Fig.13. Visualization of various LFP ridge characteristics (level I-III) on the glass surface using SO@STD NPs.

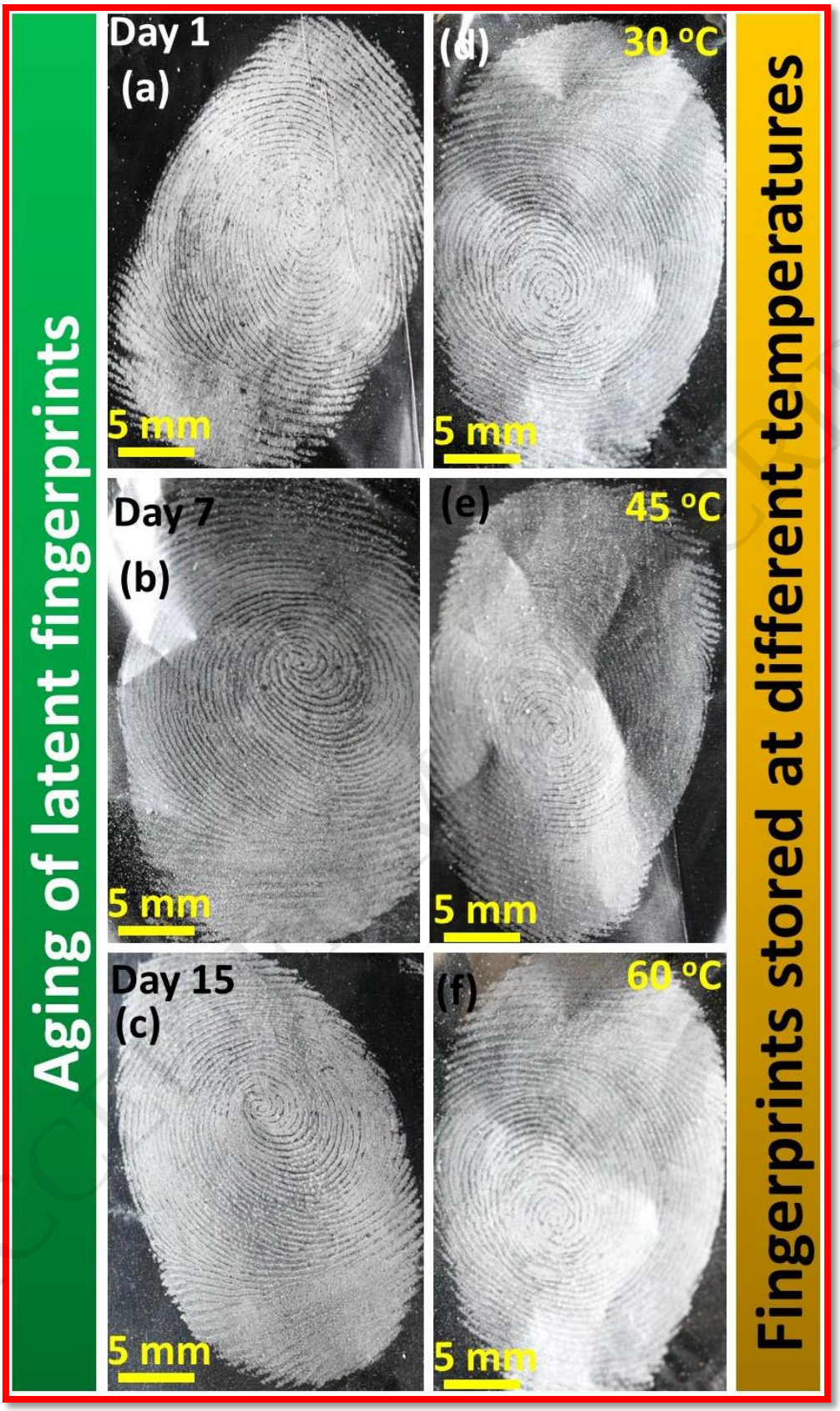

Fig.14 Visualization of LFPs (a-c) aged for various periods and (d-f) stored at different temperatures.

Table.1 Estimated average crystallite size, micro-strain and energy band gap values of STD and SO@STD NPs.

Samples	**Average crystallite size (nm)**		**Micro-strain ε (x 10^{-3})**	**E_g (eV)**
	Scherrer's method	**W-H method**		
STD	31	43	1.11	4.01
SO@STD (coat I)	31	39	1.09	4.05
SO@STD (coat II)	31	42	1.12	4.08
SO@STD (coat III)	30	31	1.15	4.15

Table.2 The effect of SiO_2 coating on the PL properties of the previously reported results.

System	Synthesis Method	PL study	Reason	Reference
$SiO_2@Y_2O_3:Eu^{3+}$	modified Stöber	Reduced	Silanol (SiO-H) group which acts as the luminescence quencher	Carrillo Romo et.al., [38]
$SiO_2@Y_2O_3:Eu^{3+}$	solid state reaction	Enhanced	Coating silica can decrease the surface defects of nanoparticles and increase their intensity	Guixia Liu et.al, [39]
$Y_2O_3:Eu^{3+}@SiO_2$	modified Stöber	Reduced	Silanol (SiO-H) group which acts as the luminescence quencher	Tong Liu et al., [40]
$SiO_2@YVO_4:Ln^{3+}$ (Ln^{3+} = Eu^{3+}, Dy^{3+}, Tm^{3+})	Sol-gel	Reduced	Silanol (SiO-H) group which acts as the luminescence quencher	Meitram Niraj Luwang et al., [41]
$SiO_2@Gd_2O_3:Eu^{3+}$	solid state reaction	Unchanged	Silica coating did not alters the crystal field of Gd_2O_3 surface	Guixia Liu et al., [42]
$SiO_2@YVO_4:Dy^{3+}/Sm^{3+}$	Sol–gel	Enhanced	Increase of the thickness $YVO_4:Dy^{3+}$/ Sm^{3+} shells on the SiO_2 cores	Wang et.al, [43]
$SiO_2@BaMgAl_{10}O_{17}:Eu^{2+}$	atomic layer deposition	Reduced	Due to SiO_2 thin film which acts as a barrier against the native oxygen	Young Kyu Jeong et.al.,[44]
$SiO_2@GdVO_4:Eu^{3+}$	Sol–gel	Enhanced	Due to the increase of the thickness of phosphor shells on the SiO_2 spheres	Guangzhi Li et.al., [45]
$SiO_2@BaMgAl_{10}O_{17}:Eu^{2+}$	solid-state reaction	Enhanced	The reduction of the surface defect density (ns) by SiO_2 coating	Sohn et.al., [46]
$SiO_2@CaMoO_4:Tb^{3+}$	modified Stöber	Enhanced	Due to the increase of the thickness of phosphor shells on the SiO_2 spheres	Guangzhi Li et.al., [47]

Table.3 Photometric properties of STD and SO@STD NPs.

Samples	CIE Coordinates		CCT values		CCT (K)	CP (%)
	x	y	u'	v'		
STD	0.319	0.242	0.183	0.410	5896	76
SO@STD (coat I)	0.358	0.237	0.199	0.424	6272	85
SO@STD (coat II)	0.358	0.248	0.201	0.462	6284	86
SO@STD (coat III)	0.358	0.261	0.212	0.481	6266	88

Table.4 Estimated trap parameters of STD and SO@STD NPs with coat-III irradiated with γ-dose in the range 1-8 kGy.

γ-dose (kGy)	Peak	T_m (K)	μ (b)	Activation Energy, E (eV)			s (s^{-1})
				Chen	Grossweiner	Luschik	
1	1	161	0.47 (2)	0.532	0.562	0.516	$5.3x10^{08}$
	2	213	0.49 (2)	0.718	0.768	0.672	$3.1x10^{11}$
2	1	159	0.49 (2)	0.424	0.450	0.488	$3.2x10^{08}$
	2	211	0.50 (2)	0.758	0.742	0.746	$2.6x10^{12}$
3	1	162	0.48 (2)	0.454	0.498	0.447	$8.3x10^{07}$
	2	209	0.48 (2)	0.749	0.819	0.732	$2.1x10^{12}$
4	1	163	0.48 (2)	0.532	0.522	0.488	$3.4x10^{08}$
	2	210	0.48 (2)	0.868	0.848	0.82	$2.4x10^{12}$
5	1	164	0.49 (2)	0.54	0.572	0.571	$6.0x10^{08}$
	2	211	0.49 (2)	0.76	0.728	0.721	$8.0x10^{12}$
6	1	163	0.49 (2)	0.69	0.624	0.692	$4.2x10^{10}$
	2	210	0.50 (2)	1.072	1.012	1.024	$7.6x10^{15}$
7	1	162	0.51 (2)	0.509	0.519	0.529	$2.4x10^{08}$
	2	208	0.47 (2)	0.672	0.642	0.624	$3.3x10^{09}$
8	1	162	0.47 (2)	0.674	0.588	0.588	$2.2x10^{09}$
	2	213	0.50 (2)	1.132	1.148	1.148	$9.2x10^{13}$

Table.5 Kinetic parameters of SO@STD NPs by CGCD method.

Heating rate (ºC/s)	**Peak 1**		**Peak 2**	
	E (eV)	**S (s^{-1})**	**E (eV)**	**S (s^{-1})**
3	0.48	$2.32x10^6$	0.98	$4.61x10^6$
4	0.45	$5.72x10^6$	0.83	$7.42x10^6$
5	0.48	$1.32x10^6$	0.96	$4.98x10^6$
6	0.52	$1.45x10^6$	1.17	$3.42x10^6$

Table.6 Kinetic parameters of SO@STD NPs by glow curve methods.

Methods	**Heating rate (ºC/s)**	**Peak 1**		**Peak 2**	
		E (eV)	**S (s^{-1})**	**E (eV)**	**S (s^{-1})**
Chen	3	0.60	$1.72x10^{6}$	0.95	$7.52x10^{9}$
	4	0.62	$9.25x10^{6}$	0.86	$9.42x10^{7}$
	5	0.65	$9.18x10^{6}$	0.92	$1.62x10^{9}$
	6	0.66	$9.06x10^{6}$	0.91	$1.22x10^{9}$
Grossweiner	3	0.55	$3.36x10^{6}$	0.96	$1.32x10^{10}$
	4	0.51	$4.42x10^{6}$	0.94	$9.48x10^{7}$
	5	0.66	$6.72x10^{6}$	0.86	$4.06x10^{8}$
	6	0.62	$6.82x10^{6}$	0.92	$3.41x10^{6}$
Luschik	3	0.58	$5.03x10^{6}$	1.08	$4.05x10^{11}$
	4	0.56	$6.72x10^{6}$	0.98	$2.56x10^{9}$
	5	0.74	$1.45x10^{6}$	1.06	$3.08x10^{8}$
	6	0.68	$1.38x10^{6}$	1.09	$3.32x10^{6}$